

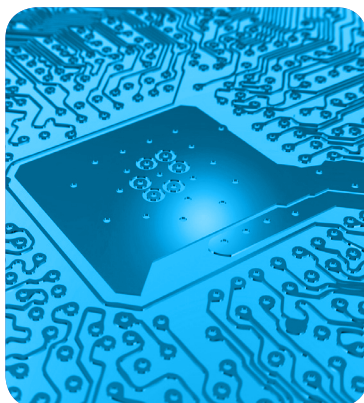
MÁSTERES de la UAM

Facultad de Ciencias
/ 14-15

Química Teórica



**Molecular
Dynamics of
aqueous $[UO_2]^{2+}$
diffusion in clays**
Sergio Pérez Conesa



Molecular Dynamics of aqueous $[\text{UO}_2]^{2+}$ diffusion in clays

Sergio Pérez Conesa¹

July 16, 2015

Supervisors: José M. Martínez.², Enrique Sánchez Marcos³

¹Departamento de Química. Universidad Autónoma de Madrid. Madrid (Spain).
sperezconesa@gmail.com

²Dept. Química Física. Universidad de Sevilla. c/ Prof. García González s/n 41012. Sevilla
(Spain) josema@us.es.

³Dept. Química Física. Universidad de Sevilla. c/ Prof. García González s/n 41012. Sevilla
(Spain) sanchez@us.es.

Abstract

Knowledge of actinide aqueous solution confined in clay interlayers are crucial when designing permanent geological high level radioactive waste facilities. The actinide ions are sealed using montmorillonite containing clays to prevent radionuclide escape. A computational study of UO_2^{2+} aqueous solution, hydration and diffusion inside montmorillonite clay was accomplished. The actinide-clay *ab initio* interaction potential was built based on the Hydrated Ion concept. It is the first time that the hydrated ion model is applied to a confined medium chemical problem. This potential was used to carry out NPT classical molecular dynamics simulations for montmorillonite- UO_2^{2+} systems with two possible interlayer water contents. Radial distribution functions, z-density profiles and translational autodiffusion constants were calculated. The aquaion showed a partial dehydration of the equatorial second hydration shell with respect to solution. No dehydration was found in the axial hydration shells. This hydration structure is caused by the alignment of the UO_2^{2+} axis with the clay surface. Formation of stable pentaquo uranyl outershell complexes was found in agreement with EXAFS studies without any external imposed constraint. The calculated translational diffusion coefficients of UO_2^{2+} are lower than in aqueous solution by a factor of five, which is within the range of values reported experimentally. This diffusion happens predominantly parallel and close to the clay surface through a hopping mechanism.

Nomenclature

DFT	Density Functional Theory.
GTF	Gaussian-Type Function.
HF	Hartree-Fock
HI	Hydrated Ion
HIC	Hydrated Ion Clay Potential Interaction.
HIW	Hydrated Ion-Water
HLRW	High Level Radiactive Waste
IMC	Intra-Molecular Cation
IW1	Ion-Water First Shell
MD	Molecular Dynamics Simulation
MP2	Moller-Plesset Perturbation Theory to the second order
MSD	Mean Square Displacement
PBC	Periodic Boundary Conditions
PES	Potential Energy Surface
QM	Quantum Mechanics
RDF	Radial Distribution Functions
RI	Resolution of The Identity.

u.c. Unit cell.

VAC Velocity Autocorrelation Function

Contents

1	Introduction	4
2	General Theory	8
2.1	Theoretical description of aqueous ion solutions.	8
2.2	The Hydrated Ion Model	11
2.3	QM Calculation Acceleration Methods	13
2.3.1	Resolution of the Identity.	14
2.3.2	The RIJCOSX technique.	15
3	Methods	17
3.1	System definition	17
3.2	Force Fields	19
3.2.1	Clay Force Field	19
3.2.2	Water and Na ⁺ Force Field	19
3.2.3	UO ₂ ²⁺ Hydrated Ion Model	20
3.2.4	Clay-[UO ₂ · (H ₂ O) ₅] ²⁺ interaction potential, the HIC interaction. . .	24
3.3	Molecular Dynamics Simulations	28
3.3.1	Molecular Dynamics Properties.	29
4	Results and Discussion	32
4.1	HIC Interaction Parameters Developed	32
4.2	Velocity Autocorrelation Functions	35
4.3	Simulation Visualizations	36
4.4	Radial Distribution	37
4.5	Z-Density Profiles	40
4.6	Translational Autodiffusion Coefficients of [UO ₂ · (H ₂ O) ₅] ²⁺ in montmorillonite	42
5	Conclusions	44

Chapter 1

Introduction

The electricity global demand has been growing since the industrial revolution of the XIX century. An alternative found to the energetic scarcity was resorting to nuclear energy as an emissionless cheap energy source. Unfortunately, this energy produces high-level radioactive waste (HLRW) that must be dealt with in a secure way. The HLRW is initially stored in nuclear plants in the form of rods inside waste pools or dry casks made of concrete. After several decades of on-site storage the spent fuel reduces its radioactivity and heat production and can be transported to a permanent geological disposal facility in which it shall be isolated permanently from the environment. The security of such facilities must be extreme since the fission products of the fuel remain hazardous for millenia. Geological disposal sites of HLRW are mined tunnels or cavities 250 to 1000 meters underground sealed and in principle isolated from the environment.¹ The main threat of these facilities is that water would reach the fuel containers corroding the radioactive material allowing its speciation and release to the environment in the form of aqueous ions.²

Aqueous actinides cations are one of the main potential hazards of a radioactive release to the environment. Their involved redox and coordination chemistry in addition to their complicated interactions with geochemical matrices³ makes their study a vast and multidisciplinary field that encompasses both experimental and theoretical research. The flagship metal of the actinide group is uranium. At the redox potential and pH of natural water, the oxidation state of U is VI, being found in the form of the uranyl cation UO_2^{2+} . In moderately acidic solution at low concentrations the dominant species is the pentagonal bipyramid $[\text{UO}_2 \cdot (\text{H}_2\text{O})_5]^{2+}(\text{aq})$ ³ with a possible (and still debated) minor octahedral tetraaquo species in equilibrium with it.⁴ The pentagonal bipyramid aquaion shall be the

focus of this research.

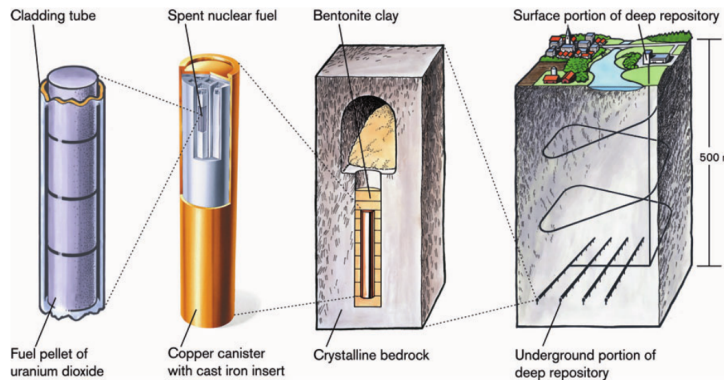


Figure 1.1: Barriers for HLRW in geological disposal facility.¹

Predicting and controlling the transport properties of uranyl when released to Nature or in the event of a container breach requires a detailed understanding of the physico-chemical peculiarities of the dynamical interaction of the cation with the matrices it may be exposed to. We consider that one of the most important of these matrices are clays and clay minerals. Clay minerals are fine grain hydrated phyllosilicates formed by cations octahedrally and tetrahedrally coordinated to oxygen or hydroxide. The term clay (as it is commonly known) is textural rather than compositional.⁵ It defines a material of particulate smaller than $2\ \mu\text{m}$ containing clay minerals and than can coexist with other mineral or amorphous phases. Their cation exchange capacity and their mechanical and plastic strength makes them ideal barrier materials for HLRW disposal facilities. Bentonite clays are used in such facilities as liner or buffer material filling the space in the repository openings between the waste material and the rock, isolating the radioactive material from the environment should it become mobile. An additional natural barrier is always present in the repositories, the rock in which the facility is located. This natural barrier should also retain and dilute the release of the radiohazards if the first barrier is passed. In some cases location of the facility is in bentonite rock.¹

Bentonite rock is an absorbent impure clay mixture composed mostly of Montmorillonite clay. Montmorillonite is an aluminosilicate consisting of Al, Fe, or Mg octahedra sandwiched between two sheets of Si tetrahedra forming layers of solid material. In between the clay layers there are hydration water layers with liquid-like dynamics and hydrated ions. This space is known as the clay interlayer. This clay mineral belongs to the smectites family which have in common a net negative charge in the clay layer that is compensated by cations in their hydrated interlayer.

The model clay to be studied is a generic sodium Montmorillonite with unit cell for-

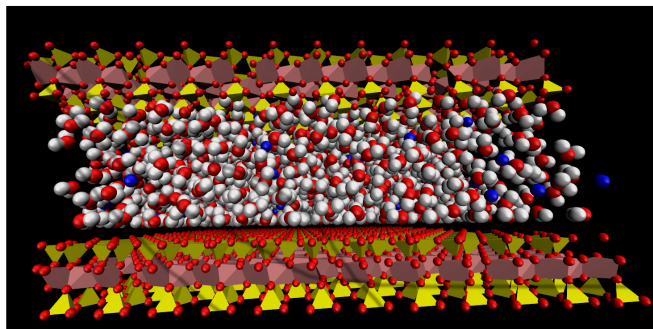


Figure 1.2: Montmorillonite section. Al or Mg Octahedra (Pink), Si tetrahedra (Yellow), O (Red), H (White) and Na (Blue)

mula $\text{Na}_{0.66}[\text{Al}_{3.33}\text{Mg}_{0.66}][\text{Si}_8]\text{O}_{20}[\text{OH}]_4 \cdot n(\text{H}_2\text{O})$. The Mg(II) atoms are isomorphic substitutions in the lattice of the Al(III) atoms in the octahedra that give the layers a net negative charge. The interlayer (also known as basal space) contains an aqueous cation solution, Na^+ in this case, that compensates the net charge of the layers. Montmorillonite is a hydrophilic clay and swells due to uptake of water from its surroundings that it absorbs in its interlayer. Therefore, there are several hydration states (different values of n) that depend on exposure to humidity. This ability to swell absorbing water can prevent (or at least hold) water from breaking in to HLRW repositories.

The main reason to use clays as barrier materials is their sorption capacity to capture cations (e.g. UO_2^{2+}) into their interlayer from the surrounding and release some cations previously inside their interlayer. This process is known as ionic exchange. There are two main sorption mechanisms: physisorption and chemisorption.³ In the first mechanism the aquaion is held within the clay particle by intermolecular forces (dispersion, H-bonds, electrostatic interactions etc.) and none of the clay atoms enter the first hydration shell. These are known as *outer-sphere complexes*. On the other hand, a chemisorbed aquaion bonds directly to clay atoms which enter and disrupt the first hydration shell. These are known as *inner-sphere complexes*. Both processes can coexist and compete.

Catalano et al.⁶ showed through EXAFS studies that $[\text{UO}_2 \cdot (\text{H}_2\text{O})_5]^{2+}(\text{aq})$ at low pH (~ 4) and low ionic strength (10^{-3}M) binds as an outer-sphere complex. The formation of this complex is inferred from the fact that the solution EXAFS of UO_2^{2+} is nearly identical to that of UO_2^{2+} adsorbed to the clay, giving in both cases the same first shell coordination numbers and distances. In contrast, at neutral pH (~ 7) and high ionic strength (1M) the equatorial solvation shell is broken and the U bonds to the clay's edge sites forming an

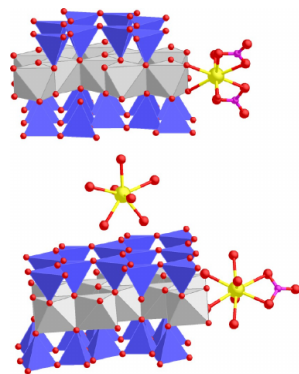


Figure 1.3: Uranyl and uranyl carbonate complexes with montmorillonite. Yellow balls are uranium, and red balls are oxygen. Montmorillonite is represented as polyhedra of SiO_4 tetrahedra (blue) and AlO_6 and FeO_6 octahedra (gray), H is omitted.³

inner sphere complex. In this case, the solution and clay EXAFS of U are different and for the mineral system the spectra reflects the existence of oxygen atoms different from O_{yl} or water O in the first hydration shell of the actinide.

There is a large number of computational studies of clay systems using molecular dynamics and Monte Carlo simulation.^{7,8} This research started 25 years ago with limited classical models due to the low computational resources available at that time.^{9,10} Nowadays, the models have reached time and lengths scales orders of magnitude higher allowing the study of representative clay systems that reproduce and explain mineralogical and chemical experimental evidence in a much more satisfactory way.

Uranyl-clay systems have been previously studied with classical simulation methods.¹¹⁻¹⁵ All of them used the empirical interaction potential model developed for aqueous UO_2^{2+} solution developed by Whipff and Guilbaud in 1993¹⁶ and Lorentz-Berzelot combination rules to reproduce the clay- UO_2^{2+} interaction. Though excellent for its time, with nowadays access to routine quantum chemical calculations better classical force fields based on *ab initio* methods can be developed to obtain more realistic molecular dynamics simulations.

The aim of this project is to develop an improved interaction potential for the system. Then the classical dynamics of $[\text{UO}_2 \cdot (\text{H}_2\text{O})_5]^{2+}(\text{aq})$ in the aqueous interlayer will be studied to gain understanding of this technologically relevant phenomenon using molecular dynamics simulations (MD) .

Chapter 2

General Theory

2.1 Theoretical description of aqueous ion solutions.

The study of aqueous electrolyte solutions was one of the first areas of Physical Chemistry developed by prestigious scientists such as Arrhenius, Born, Debye, Hückel and Onsager.¹⁷ Their properties were rationalized using electrolyte dissociation theory and classical electric polarization models. This formed the basis of Ionic Electrochemistry, considered a classical discipline in Physical Chemistry.¹⁸ In the 70s of the last century, metal ions became particularly relevant into the area of Coordination Chemistry being the key component of metal coordination complexes.¹⁹ The role of metal ions in Biology, Biomedicine, Metallurgy, Nuclear Technology, Environmental Science among other disciplines is present in contemporary Chemistry.¹⁸⁻²³

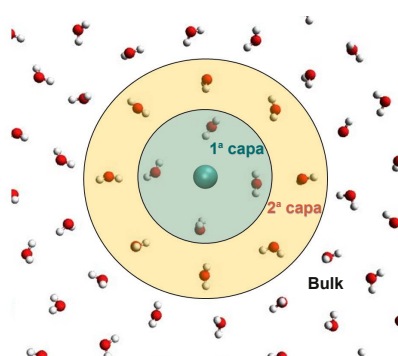


Figure 2.1: Frank and Evans concentric shell model.

Aquaions with a general formula of $[M(H_2O)_n]^{m+}(aq)$ are the structures adopted by M^{m+} in aqueous solution assuming no hydrolysis or polymerization products are formed. The physical chemistry of aquaion containing solutions is governed by the net charge of the complex, $m+$ and the polarizable nature of the water molecules. The electrostatic effects for these systems are so strong that they extend out of the aquaion defining different solvation shells around the central metal cation. This hydration structure was proposed by Frank and Evans and is known as the *concentric shell model*²⁴ (see Figure 2.1).

Description of highly-charged metal cation in aqueous solutions requires complex theoretical approximations due to the contribution of the strong and long-range electrostatic interactions with the water structure. The polarizing capability of such ions is high, strongly influencing the geometry and wavefunction of the first shell of water molecules which are bonded to the metal. For this reason only through a quantum mechanical (QM) approach we can study the interactions and bonding in the system. Additionally, due to the long-range nature of the electrostatic interactions, the second and outer hydration shells are also affected requiring to model the presence of the solvent in the system. The simplest model to deal with this issue is the continuum solvation model, included in the QM calculation, for example PCM.²⁵ Unfortunately, continuum solvation methods lose all micro-structural information related to the hydration shells replaced by the continuum. The only apparent solution would be to include in the QM system a given number of hydration shells, then becoming a semicontinuum solvation model although this would greatly increase the expense of the calculations, among other problems.²⁶

To study the dynamics of metal cations in aqueous solution or inside a clay mineral, the ideal simulation method is some QM-based molecular dynamics method, such as Car-Parrinello or Born-Oppenheimer molecular dynamics. These methods can include periodic boundary conditions (PBC) which make the system “infinite”. But PBC come at the cost of the inclusion of an artificial periodicity not present in liquids that can become important if the simulation box is too small. The high computational cost of the accurate solution of the Schrödinger equation or the Kohn-Sham equations to calculate the forces on the atoms limits strongly the system size and the simulation time spanned.

Classical molecular dynamics and other classical mechanics-based methods have shown to be able to predict solution properties.^{27,28} The simulation length and timescales available to these methods are superior to QM-MD methods in a large extent. The price to pay for the speed of the technique is that, the model and the model’s interactions are not derived from on-the-fly QM information, having to be chosen carefully to avoid meaningless results. In addition, the bonding of such systems is fixed *a priori* and cannot change during the simulation.

In most cases, non-polarizable classical potential interactions are site-site (pairwise) which in principle cannot reproduce explicitly the many body effects present in the true interactions unlike QM-MD. Nevertheless, there is an intermediate possibility between QM and non-polarizable classical models which is polarizable classical force fields. In this case, the polarization of the molecules as a function of the environment reproduces the polarization present in QM interactions explicitly, which is one of the main many-body interactions. Unfortunately, they are computationally more expensive and polarizable interactions do not allow introducing first shell-ion charge transfer which is present in the UO_2^+ aquaion.

In the early days of classical simulations, interaction potentials were defined by empirical analytical functions with parameters fitted to reproduce experimental data. When routine QM calculations became available, potentials were developed to reproduce the QM interactions. Thus, the transferability of the potentials out of the range in which they were fitted was increased significantly. *Ab initio* potential development allows a progressive quality increase by improving the level of theory of the electronic structure method, the number and geometry of structures included and the system size.

Even if classical interaction potentials are based on QM calculations, force fields are in most cases pairwise and based on the interaction of isolated fragments (the ion and a single water molecule). This method is inadequate to study cation-polar solvent interactions. One of the problems of this description is an overestimation of the interaction as a consequence of the electrical polarization of the solvent by the cation. Also, for high charge cations, the true dissociation limit of the aggregate $[\text{M}(\text{H}_2\text{O})_n]^{m+}$ is the charge transfer state $\text{M}^{(m-1)+} + \text{H}_2\text{O}^+$ instead of the expected $\text{M}^{m+} + \text{H}_2\text{O}$, as a consequence of the relative values of the ionization energy of the water molecule and the electron affinity of the metal.²⁹ In addition, *d* and *f* series metals with partially filled orbitals are perturbed differently by water molecules depending on the water-ion distance possibility altering its electronic state.

In this project we will present classical non-polarizable MD simulations which satisfy the time and length scales of the phenomena of interest. We will use QM calculations as a benchmark to parametrize the interaction potential and thus capture the essence of the major electronic effects (polarization, many body effects...) in an implicit way. To avoid the known problems associated to the interaction of isolated fragments when studying metal-water interactions we will make use of the Hydrated Ion Model .

2.2 The Hydrated Ion Model

The generally used way to model ion water interactions in classical MD is to represent the ion as a charged particle with a Lennard-Jones potential to incorporate dispersion interactions (a “charged soft sphere” model). All water molecules of the system are identical independently of the distance to the ion and the water model is fitted to reproduce the bulk properties of liquid water. The ion-water interaction is represented by a coulomb interaction and a Lennard-Jones potential (Equation 2.1) making use of the Lorentz-Berzelot combination rules (Equation 2.2). Therefore, the interactions are obtained by combining the properties of the individual particles and not from the complex interaction directly. This model has the advantage of being very simple to implement and satisfactory if the ions are not the subject of study, for example if they are background ions as statistical theory of liquid state shows. Nevertheless, it gives a very limited description of the system if any detail of the microstructure of the solvation of the ion wants to be studied.

$$E_{ij}^{\text{vdW}}(r) = 4\varepsilon_{ij} \left[\left(\frac{\sigma_{ij}}{r} \right)^{12} - \left(\frac{\sigma_{ij}}{r} \right)^6 \right] \quad (2.1)$$

$$\varepsilon_{ij} = \sqrt{\varepsilon_{ii}\varepsilon_{jj}} \quad \sigma_{ij} = \frac{\sigma_{ii} + \sigma_{jj}}{2} \quad (2.2)$$

The research group where this project was carried out, proposed more than twenty years ago to incorporate the classical concept of the hydrated ion (HI) to the development of classical cation-water force fields.³⁰ Fundamental idea of the HI model is to consider the cation and its first hydration shell as the interacting entity with the bulk water molecules of the solvent. This allows us to treat the first hydration shell in a completely different manner having different charges, geometries, atom types and interaction parameters than the rest of water molecules in the system which are modeled as bulk waters. This model avoids the problems associated to isolated-fragment based potentials and also gives a more detailed description of the solvation than combination-rule based force fields. Furthermore, it allows the introduction of the partial charge transfer from the cation to the first shell water molecules (although the charges are set *a priori* and do not change) and includes in the parametrization the many body effects of QM implicitly.

To define the interaction of the hydrated ion and the rest of the solvent the HIW (Hydrated Ion-Water) potential is parametrized. This interaction potential has as a reference the hydrated ion in its minimum energy geometry and the water molecule in the solvent

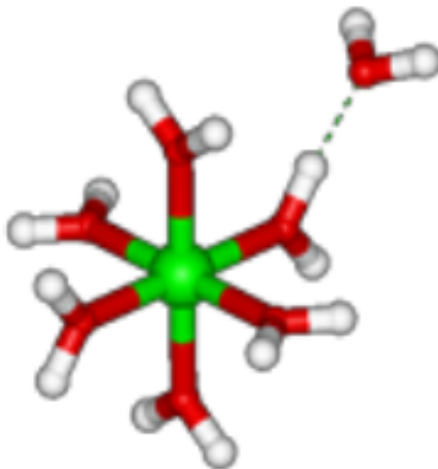


Figure 2.2: Example calculation to construct a HIW potential.

model geometry.³¹ The potential energy hypersurface (PES) of interaction of the hydrated ion and a water molecule $[M(H_2O)_n]^{m+} - H_2O$ is sampled. These interaction energies are then fitted to analytical functions of the site-site distances.

The first implementations of the model only incorporated the HIW and the hydrated ion was modeled as a rigid body in the QM optimized geometry. To allow intra-molecular motion in the aqua ion an additional potential was developed to describe the interaction of the cation with its first hydration shell, know as IW1 (Ion-Water First Shell) .

For poliatomic cations like UO_2^{2+} an extra partition of the system can be done by describing the intra-molecular interactions and dynamics of the hydrated ion. This is done by defining the IMC (Intra-Molecular Cation) .

Even though an exchangeable HI model potential has been developed³²⁻³⁴ for several systems, the residence time of H_2O in $[UO_2 \cdot (H_2O)_5]^{2+}(aq)$ is longer than the timescales than can be spanned by a simulation. Therefore, the first hydration shell is fixed *a priori* according to the experimental evidence and the water molecules will not diffuse out of its initial shell due the slow kinetics of the water exchange process.

This partitioning of the $[UO_2 \cdot (H_2O)_5]^{2+}(aq)$ system is reminiscent of the classical Frank-Evans model (see Figure 2.3).²⁴ For a system composed of the hydrated ion in water the total energy would be:

$$E_{\text{int}} = E_{\text{IMC}} + E_{\text{IW1}} + E_{(\text{W-W})_{\text{1st-shell}}} + E_{\text{HIW}} + E_{(\text{W-W})_{\text{bulk}}} \quad (2.3)$$

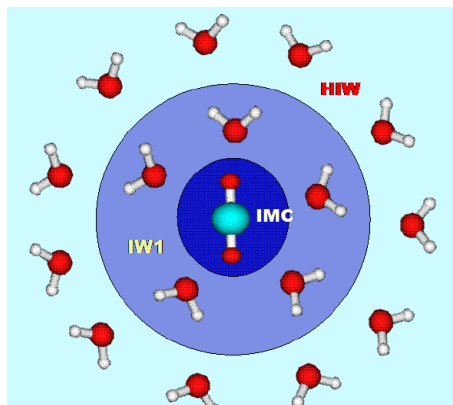


Figure 2.3: $\text{UO}_2^{2+}(\text{aq})$ interaction regions within the solution.³⁵

There are some of molecular dynamics studies of aqueous UO_2^{2+} inside montmorillonite interlayers or pores.^{11–15} All of them are based on “charged sphere models” and combination rules interactions for the clay- UO_2^{2+} and UO_2^{2+} - H_2O interactions. The delicate compromise among the layered silicates, water and uranyl cation interactions suggest a significant contribution of many-body effects in this complex system, which hardly can be fulfilled by combination rules. In particular, the interactions of the doubly charged actinyl with the clay and water. Using the hydrated ion model we expect to represent a realistic flexible model of UO_2^{2+} in solution that solves many of the known problems of the cation water interactions. This project’s goal is to develop, on the basis of the previously constructed HI model of $[\text{UO}_2 \cdot (\text{H}_2\text{O})_5]^{2+}$, a first principles clay- $[\text{UO}_2 \cdot (\text{H}_2\text{O})_5]^{2+}$ interaction potential to be used in classical molecular dynamics simulations.

2.3 QM Calculation Acceleration Methods

In this project, Moller-Plesset perturbation theory to the second order (MP2) was used in all QM calculations. This technique scales approximately as M^5 where M is the number of primitive gaussian-type functions (GFTs). This is a prohibitive cost for medium to large molecular systems like those we were faced with. For this reason we need to use some approximations that while introducing small but manageable errors reduce the computational cost of our calculations.

2.3.1 Resolution of the Identity (RI).

The main idea of the Resolution of the Identity technique³⁶ is to decompose 4 index molecular orbital electronic integrals or GTF electronic integrals into a sum of the product of 3 index integrals:

$$\langle \mu\lambda | \nu\sigma \rangle = \sum_{\kappa}^{M_{\kappa}} L_{\mu\nu\kappa} L_{\lambda\sigma\kappa} \quad (2.4)$$

Since the product of two gaussian functions produces another gaussian function, the integral can be described as the product of gaussian functions $\Omega_{\mu\nu}$:

$$\langle \mu\lambda | \nu\sigma \rangle = \left\langle \Omega_{\mu\nu} \left| \frac{1}{r_{12}} \right| \Omega_{\lambda\sigma} \right\rangle = \iint \Omega_{\mu\nu}(r_1) \frac{1}{r_{12}} \Omega_{\lambda\sigma}(r_2) d\tau_1 d\tau_2 \quad (2.5)$$

The RI method is based on the description of $\Omega_{\mu\nu}$ as a linear combination of one electron auxiliary basis set functions $\eta(r)$:

$$\Omega_{\mu\nu}(r) = \sum_Q c_{Q,\mu\nu} \eta(r) \quad (2.6)$$

It can be shown that the optimal $c_{Q,\mu\nu}$ are :

$$c_{Q,\mu\nu} = \sum_P \left\langle \Omega_{\mu\nu} \left| \frac{1}{r_{12}} \right| \eta_P \right\rangle V_{PQ}^{-1} \quad (2.7)$$

Where V_{PQ}^{-1} is the representation of the operator $\frac{1}{r_{12}}$ in the auxiliary basis set. Finally, replacing $V_{PQ}^{-1} = \sum_{\kappa} V_{P\kappa}^{-1/2} V_{\kappa Q}^{-1/2}$, we obtain the desired decomposition:

$$\begin{aligned}
\langle \mu\lambda | \nu\sigma \rangle &= \sum_P \sum_Q \left\langle \Omega_{\mu\nu} \left| \frac{1}{r_{12}} \right| \eta_P \right\rangle V_{PQ}^{-1} \left\langle \eta_Q \left| \frac{1}{r_{12}} \right| \Omega_{\lambda\sigma} \right\rangle \\
&= \sum_{\kappa} \left(\sum_P \left\langle \Omega_{\mu\nu} \left| \frac{1}{r_{12}} \right| \eta_P \right\rangle V_{P\kappa}^{-1/2} \right) \left(V_{\kappa Q}^{-1/2} \left\langle \eta_Q \left| \frac{1}{r_{12}} \right| \Omega_{\lambda\sigma} \right\rangle \right) \quad (2.8) \\
&= \sum_{\kappa}^{M_{\kappa}} L_{\mu\nu\kappa} L_{\lambda\sigma\kappa}
\end{aligned}$$

This technique is exact for an infinite auxiliary basis set, unfortunately we must work with finite basis sets that introduce some numerical error. The auxiliary basis sets are built for each regular basis to maximize accuracy and its completeness while minimizing the number of auxiliary basis functions. They can also be built on-the-fly by some programs.

The RI decomposition of integrals can be used to reduce the scaling of the calculation of the coulomb operator and the $\langle ab | rs \rangle$ molecular integrals of MP2 making accessible otherwise prohibitive calculations. It is also useful to decompose the exchange operator but the scaling is not affected. Nevertheless, its decomposition is useful for integral screening purposes reducing the scaling prefactor.

The RI decomposition was used in our calculations to compute the second order correction to the energy. For the initial Hartree-Fock (HF) calculation, the RIJCOSX technique, more suited for such method, was used.

2.3.2 The RIJCOSX technique.

The RIJCOSX technique was developed by Nesse and coworkers³⁷ to encompass the scaling capability of RI, the speed of seminumerical integral calculation of pseudospectral methods and potent integral screening criteria.

Pseudospectral techniques³⁸ are based on performing numerical integration on one of the electron coordinates while keeping analytical integration for the second. Integration over r_1 is replaced by a sum over a set of grid points $\{r_g\}$:

$$\langle \mu\lambda | \nu\sigma \rangle = \iint \Omega_{\mu\nu}(r_1) \frac{1}{r_{12}} \Omega_{\lambda\sigma}(r_2) d\tau_1 d\tau_2 \approx \sum_g \Omega_{\mu\nu}(r_g) \int \frac{1}{|r_g - r_2|} \Omega_{\lambda\sigma}(r_2) d\tau_2 \quad (2.9)$$

And expanding $\Omega_{\mu\nu}$:

$$\langle \mu\lambda | \nu\sigma \rangle \approx \sum_g \phi_\mu(r_g) \left[\int \frac{1}{|r_g - r_2|} \Omega_{\lambda\sigma}(r_2) d\tau_2 \right] \phi_\nu(r_g) = \sum_g \phi_\mu(r_g) A_{\lambda\sigma}(r_g) \phi_\nu(r_g) \quad (2.10)$$

Where $A_{\lambda\sigma}(r_g)$ are one electron three center integrals over the grid. As these integrals combine spectral and physical grid elements they are known as pseudospectral integrals. It can be shown that they are able to reduce the scaling of the computation of both the exchange and coulomb operators if the number of grid points is not very large. Therefore, the grid must be balanced to reduce the computational cost, having as less points as possible, without compromising too much accuracy.

RIJCOSX is a complex technique that uses RI to approximate the coulomb operator and sophisticated pseudospectral computation methods for multicenter integrals of the exchange operator. The acronym comes out of: **RI** on **J** (Coulomb) and **Chain of Spheres on X** (exchange). Chains of spheres is one of the powerful pseudospectral integral screening criteria used in the method. RIJCOSX has demonstrated to reduce significantly the scaling of HF and hybrid functional DFT calculations.

It is important to be cautious when using RI and RIJCOSX acceleration, like when applying any approximation. They introduce numerical errors that could be important for accurate calculation. Nevertheless, these are typically smaller than other sources of error (specially for RI) like basis set incompleteness, basis set superposition error and in our case force field fitting. In addition, their errors have been found to be relatively systematic and error cancellation can mitigate the accuracy loss.

Chapter 3

Methods

3.1 System definition.

The system we are going to simulate using classical MD is a Na-montmorillonite clay in which a small fraction of the Na^+ ions is substituted by $[\text{UO}_2 \cdot (\text{H}_2\text{O})_5]^{2+}$ hydrated ions to represent a possible scenario of actinide interaction with liner material in a HLRW disposal facility. The montmorillonite structure is derived from a triclinic pyrophyllite structure from the literature³⁹ based on X-ray diffraction. H atom positions have been assigned by means of *ab initio* calculations. Lattice parameters are given in Table 3.1. The value of c will depend on the hydration state that is being simulated.

Table 3.1: Unit cell parameters of pyrophyllite modeled by Bickmore et al.³⁹

$a(\text{\AA})$	$b(\text{\AA})$	$c(\text{\AA})$	$\alpha(^{\circ})$	$\beta(^{\circ})$	$\gamma(^{\circ})$
5.1488	8.9979	9.8409	91.2047	100.7358	89.6576

To obtain the montmorillonite structure we apply random isomorphic octahedral substitutions of Al^{3+} by Mg^{2+} outlawing the possibility of substituting two vertex-sharing octahedra to fulfill Loewenstein's rule.⁴⁰ The formula per unit cell used was $\text{Na}_{0.66}[\text{Al}_{3.33}\text{Mg}_{0.66}][\text{Si}_8]\text{O}_{20}[\text{OH}]_4 \cdot n(\text{H}_2\text{O})$. The simulation box will contain two interlayers and two clay layers displaced by \vec{c} . Each clay layer will consist of a 9×5 supercell (of size $\sim 47 \times 45 \text{\AA}^2$). The two interlayers contain the hydration water molecules and the Na^+ that balance the negative charge of the layers. Two Na^+ atoms and 5 H_2O will be substituted of each interlayer by $[\text{UO}_2 \cdot (\text{H}_2\text{O})_5]^{2+}$. Thus, each simulation box will contain 2 uranyl aquaions to double the statistical significance of the calculated properties but

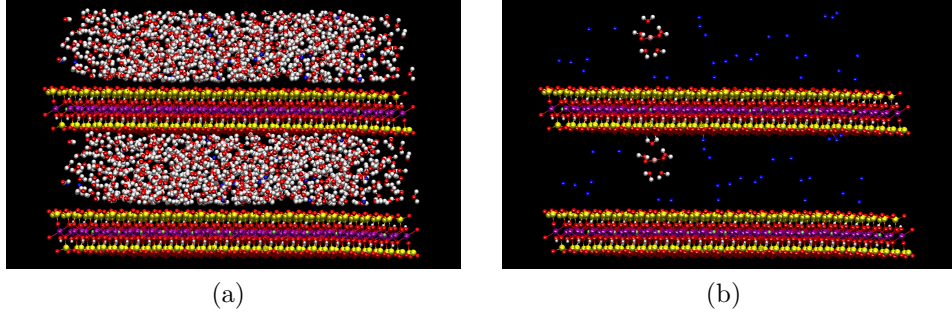


Figure 3.1: (a) Simulation boxes under study. H (white), O (red), Na (blue), Mg (green), Al (purple), Si (yellow), U (pink). (b) Same system but omitting the H_2O .

avoiding short range aquaion-aquaion interaction. An example of the systems simulated can be seen in Figure 3.1.

The interlayer or basal space of Na-montmorillonite may contain from 1 to 4 average monolayers of water molecules (designed hereafter 1W-4W hydration states) depending on the nature of the interlayer solution and the conditions of T,P, humidity and previous history of the clay. In the four states the basal spacing, d_{001} has been measured experimentally but the amount, n , of water molecules per unit cell (u.c.) is unknown. Holmboe et al.'s molecular dynamics simulations with 5 H_2O molecules per unit cell and per hydration state reproduce the experimental d_{001} (See Figure 3.2).⁴¹ In our simulations we used their criterion to fill with water molecules the interlayer and we took the initial d_{001} from experiment.⁴² We will focus our attention on hydration states 3W and 4W.

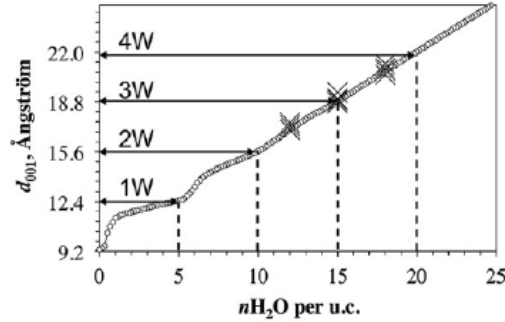


Figure 3.2: Simulated d_{001} as a function of $n\text{H}_2\text{O}$ per unit cell. from NPT molecular dynamics simulations.⁴¹ Experimental X-Ray diffraction d_{001} values of the 1W,2W,3W, and 4W hydration states of a Wyoming type Na-montmorillonite are shown as horizontal arrows.⁴²

3.2 Force Fields

In this section we shall detail the set of atom types and interaction potentials of the system, which are commonly known as the force field of the system.

3.2.1 Clay Force Field

The montmorillonite force field is the CLAYFF force field.⁴³ It was developed specifically to treat hydrated and multicomponent mineral systems and their interface with aqueous solution. This force field assigns to each atom type a partial charge and Lennard-Jones parameters. The Lorentz-Bertzelot combination rules are used to model the van der Waals interaction of atoms with different atom types (unless they belong to $[\text{UO}_2 \cdot (\text{H}_2\text{O})_5]^{2+}$). The force field gives equal van der Waals interactions to all atom types of an element and particularizes the charge as a function of the surroundings of the atom type in the clay. For example, the force field gives different charges to bridging oxygens of polyhedra and hydroxyl oxygens. It further distinguishes between oxygen or hydroxyl oxygen that form part of a regular polyhedron or a substituted polyhedron. The model gives for Si, Al and Mg atoms very small ϵ_{ii} Lennard-Jones parameters making these atoms practically charged hard spheres. The only bonded unit in the force field is the hydroxyl O-H bond which will be treated as a rigid unit at the equilibrium bond length of the force field, 1.0 Å.

3.2.2 Water and Na^+ Force Field

The CLAYFF was developed using the SPC water model.⁴⁴ Even though, this would be the ideal water model to use in combination with it, for compatibility reasons with the HI model interactions of uranyl, Jorgensen et al.'s TIP4P model was used.⁴⁵ Several simulations have been run without uranyl using TIP4P in the interlayer of the montmorillonite. The dynamics and structural properties of these simulations are very similar to those given by the SPC model.

The TIP4P water model has the experimental geometry of liquid water but incorporates a massless auxiliary particle, q at the angle bisector 0.15 Å away from the oxygen atom (See Figure 3.3). The molecule was treated as a rigid body in the simulation. Partial charges are assigned to the H atom and q but not to the O atom. Lennard-Jones

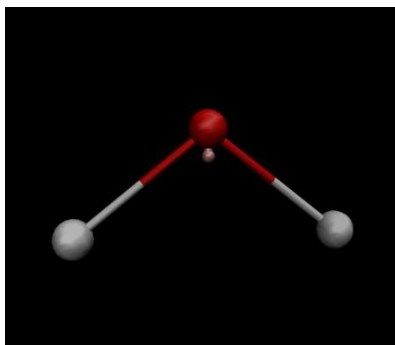


Figure 3.3: TIP4P H_2O structure $r_{\text{OH}} = 0.9572\text{\AA}$, $r_{\text{Oq}} = 0.15\text{\AA}$ and $\widehat{\text{HOH}} = 104.52^\circ$.

parameters are assigned exclusively to the O atom but taking into account the added bulk that the presence of the H provides.

From the many “charged soft sphere” models of Na^+ available in the literature, the one developed by Jorgensen et al. was chosen since it was built using TIP4P water.⁴⁶ The reason to use a simpler model for Na^+ than for UO_2^{2+} is that we are only interested in it as a background electrolyte, and the Na^+ aquaion does not satisfy the stability conditions of uranyl, as it exchanges water molecules of its first shell easily.

For both water and Na^+ their van der Waals interaction with other atom types was modeled using Lorentz-Bertzelot combination rules except for their interactions with the uranyl aquaion since these require the special treatment of the HI model. Furthermore, the van der Waals interaction of Na^+ and $[\text{UO}_2 \cdot (\text{H}_2\text{O})_5]^{2+}$ is neglected since the concentration of ions in the basal space is not high enough to force both cations close together overcoming their electrostatic repulsion.

3.2.3 UO_2^{2+} Hydrated Ion Model

To our knowledge there is only one standard force field for UO_2^{2+} . It was developed in 1993 by Whipff and Guilbaud.¹⁶ It was a naked ion model rather than HI model so parameters were constructed only for the cation and the intermolecular interactions were defined by means of Lorentz-Bertzelot combination rules. The parameters were chosen to reproduce the fivefold coordination of U and other experimental information. Thought good for its time or for less detailed description, a better force field for aqueous UO_2^{2+} can be developed. Today’s QM calculations give the possibility of developing a more sophisticated force field based on the useful idea for the HI, a new interaction potential, HI model, where the

strong clay-doubly charged cation interaction can be damped by the presence of solvent molecules.

The HI model for $[\text{UO}_2 \cdot (\text{H}_2\text{O})_5]^{2+}$ among other actinides in water solution was developed in the group.³⁵ The model was proven to satisfactorily reproduce several experimental properties such as vibrational frequencies, autodiffusion coefficient, hydration energy etc., while giving interesting insights into the nature of the aquaion.

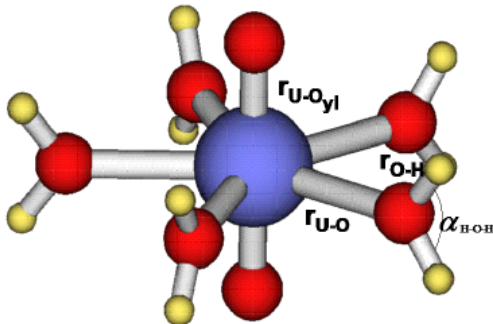


Figure 3.4: Optimized pentagonal bipyramid structure of $[\text{UO}_2 \cdot (\text{H}_2\text{O})_5]^{2+}$ at the B3LYP level of theory.

Table 3.2: $[\text{UO}_2 \cdot (\text{H}_2\text{O})_5]^{2+}$ optimized geometrical parameters for the D_{5h} symmetry.

$r(\text{U-O})$ (Å)	2.498
$r(\text{U-O}_{yl})$ (Å)	1.748
$\alpha(\text{O}_{yl}\text{-U-O}_{yl})$ ($^\circ$)	180.0
$r(\text{O-H})$ (Å)	0.970
$\alpha(\text{H-O-H})$ ($^\circ$)	106.6

The QM calculations were all carried out using *Gaussian09*.⁴⁷ The employed method was Density Functional Theory using the B3LYP functional. The U atom is described by using a Stuttgart semirelativistic pseudopotential (SDD)⁴⁸ that replaces 60 core electrons, the rest are treated explicitly with the basis functions [14s13p10d8f6g][10s9p5d4f3g]. For the H and O atoms aug-cc-pVDZ basis sets were used.⁴⁹

The basis of the model is the optimized structure of $[\text{UO}_2 \cdot (\text{H}_2\text{O})_5]^{2+}$ with pentagonal bipyramid geometry imposing D_{5h} symmetry (See Table 3.2 and Figure 3.4). Using this structure, the wavefunction is polarized using PCM²⁵ to include the average effect of the continuum dielectric solvation. The electrostatic potential generated by the wavefunction is used to fit the effective atomic charges of the hydrate using the CHELP scheme (Table 3.3).⁵⁰ The effective charges remained fixed during the rest of fitting procedures.

Table 3.3: Effective CHELPG charges of $[\text{UO}_2 \cdot (\text{H}_2\text{O})_5]^{2+}$.

	a.u.
q_{U}	2.8009
q_{O}	-1.0489
$q_{\text{O}_{\text{vi}}}$	-0.5457
q_{H}	0.5535

The PCM method is only applied to obtain the charges, but not to calculate the interaction energies because polarization effects of the bulk solvent on the hydrated ion should impact mostly its charges and not its van der Waals interactions. For the case of the HIW in which there is solvent-solute electric polarization, since the atomic charges are fixed this polarization is incorporated implicitly in the non electrostatic terms of the fit. In this way, we avoid the double counting of terms that would be present if we used in all QM calculations.

IW1 potential construction.

First of all, the IW1 potential is built by calculating the interaction energies defined in Equation 3.1 for a series of 150 structures, i , of $[\text{UO}_2 \cdot (\text{H}_2\text{O})_5]^{2+}$. In these structures, the aquaion is deformed by performing radial scans of one of the $(\text{H}_2\text{O})_1$ molecules moving away from the U atom in their hydrate minimum geometry and deformations of the UO_2^{2+} cation along its vibrational normal modes (asymmetric and symmetric tensions and bending). The first hydration shell water-water contribution of the structure is subtracted to obtain E_{IW1} . The water-water interaction is modeled with the charges of Table 3.3 and the Lennard-Jones parameters of TIP4P water. Finally, the E_{IW1} is fitted to a site-site r^n polynomial plus the electrostatic interaction (Equation 3.3). The standard deviation of the fit is lower than 1 kcal mol^{-1} .

$$E_{\text{int}}^i = E_{[\text{UO}_2 \cdot (\text{H}_2\text{O})_5]^{2+}}^i - E_{[\text{UO}_2]^{2+}}^i - 5E_{(\text{H}_2\text{O})_1} \quad (3.1)$$

$$E_{\text{IW1}} = E_{\text{int}} - E_{(\text{H}_2\text{O})_1 - (\text{H}_2\text{O})_1} \quad (3.2)$$

$$E_{\text{IW1}} = \sum_i^{\text{O}_1 \text{ sites}} \frac{C_4^{\text{UO}}}{r_{\text{UO}}^4} + \frac{C_6^{\text{UO}}}{r_{\text{UO}}^6} + \frac{C_8^{\text{UO}}}{r_{\text{UO}}^8} + \frac{C_{12}^{\text{UO}}}{r_{\text{UO}}^{12}} + \sum_i^{\text{H}_2\text{O sites}} \frac{q_{\text{U}} q_i}{r_{\text{U}i}} \quad (3.3)$$

IMC potential construction.

For the IMC interaction potential the U-O_{y1} interaction had to be computed in the presence of the first hydration shell which affects greatly the UO₂²⁺ wavefunction modifying its interaction. Thus, we model the interactions of UO₂²⁺ embedded in the hydrate. This was done by initially calculating the total interaction energy:

$$E_{\text{int}}^{\text{tot}} = E_{[\text{UO}_2 \cdot (\text{H}_2\text{O})_5]^{2+}}^i - E_{\text{U}^{6+}} - 2E_{\text{O}^{2-}} - 5E_{(\text{H}_2\text{O})_1} \quad (3.4)$$

where (H₂O)₁ represents a water molecule with the gas phase optimized geometry in the uranyl pentahydrate. This energy has three components:

$$E_{\text{int}}^{\text{tot}} = E_{\text{IMC}} + E_{\text{IW1}} + E_{(\text{H}_2\text{O})_1 - (\text{H}_2\text{O})_1} \quad (3.5)$$

Rearranging we obtain the energy expression for E_{IMC} , that was fitted to the same geometrical structures as the IW1.

$$E_{\text{IMC}} = E_{\text{int}}^{\text{tot}} - E_{\text{IW1}} - E_{(\text{H}_2\text{O})_1 - (\text{H}_2\text{O})_1} \quad (3.6)$$

The IMC potential was fitted to a functional form similar to IW1, Equation 3.7. The standard deviation of this fit was lower than 3.5 kcal mol⁻¹. If only structures with energy lower than 15 kcal mol⁻¹ are considered the standard deviation becomes lower than 0.5 kcal mol⁻¹.

$$E_{\text{IMC}} = \sum_i^{\text{O}_{y1} \text{ sites}} \frac{C_4^{\text{UO}_{y1}}}{r_{\text{UO}_{y1}}^4} + \frac{C_6^{\text{UO}_{y1}}}{r_{\text{UO}_{y1}}^6} + \frac{C_8^{\text{UO}_{y1}}}{r_{\text{UO}_{y1}}^8} + \frac{C_{12}^{\text{UO}_{y1}}}{r_{\text{UO}_{y1}}^{12}} + \sum_i^{\text{O}_{y1} \text{ sites}} \frac{q_{\text{U}}q_{\text{O}_{y1,i}}}{r_{\text{UO}_{y1,i}}} \quad (3.7)$$

HIW potential construction.

Finally, the HIW potential was developed using the [UO₂ · (H₂O)₅]²⁺-H₂O PES sampled by performing 1000 calculations on the grid derived from Figure 3.5 including different orientations of the second-shell water molecule for each point. In this case, the HIW energy expression is simply the hydrate-water interaction (Equation 3.8) and like in the previous potentials is fitted to a site-site $\frac{A}{r^n}$ polynomial plus the electrostatic interaction

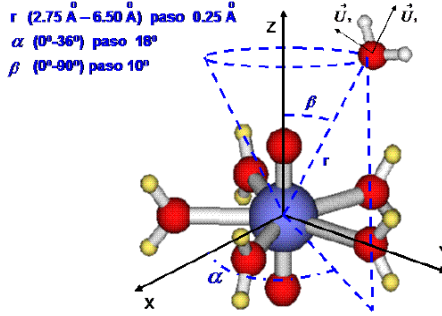


Figure 3.5: $[\text{UO}_2 \cdot (\text{H}_2\text{O})_5]^{2+}$ - H_2O OPES sampling grid to generate the HIW interaction potential.

(Equation 3.9). The standard deviation of this fit was lower than 2 kcal mol^{-1} when all the points fitted are included.

$$E_{\text{int}}^{\text{tot}} = E_{[\text{UO}_2 \cdot (\text{H}_2\text{O})_5]^{2+} - \text{H}_2\text{O}} - E_{[\text{UO}_2 \cdot (\text{H}_2\text{O})_5]^{2+}} - E_{\text{H}_2\text{O}} \quad (3.8)$$

$$E_{\text{HIW}} = \sum_i^{\text{Water sites}} \sum_j^{\text{HI sites}} \frac{C_4^{ij}}{r_{ij}^4} + \frac{C_6^{ij}}{r_{ij}^6} + \frac{C_8^{ij}}{r_{ij}^8} + \frac{C_{12}^{ij}}{r_{ij}^{12}} + \frac{q_i q_j}{r_{ij}} \quad (3.9)$$

3.2.4 Montmorillonite $[\text{UO}_2 \cdot (\text{H}_2\text{O})_5]^{2+}(\text{aq})$ interaction potential, the HIC interaction.

To our knowledge, Molecular dynamics simulations of UO_2^{2+} -containing montmorillonite systems have been carried out in all cases the UO_2^{2+} cation has been described using the model developed by Whipff¹⁶ and the Lorentz-Bertzelot combination scheme. A hydrated ion-clay interaction was developed with the aim to build a first-principles model in the new intermolecular potential, that we denote as the Hydrated Ion-Clay potential (HIC) .

The challenge of this model is that we would have to simultaneously fit the interaction between the atoms of the hydrated ions and a big number of atoms in a solid surface. There are several significant differences in the potential developed with respect to the previous potentials developed by the group. First of all the symmetry of the interaction is not close to spherical like in the HIW case. Additionally, the surface of the clay presents different interaction sites. Finally, the cost of studying these interactions will be very high due to the large number of atoms of the clay requiring some modeling decisions.

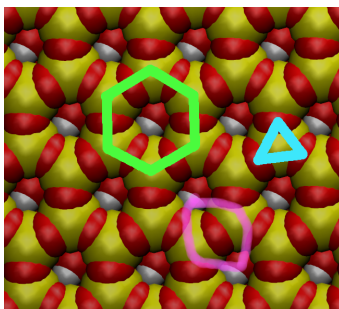


Figure 3.6: Montmorillonite surface sites for uranyl interaction: hexagonal,triangular and direct oxygen interaction.

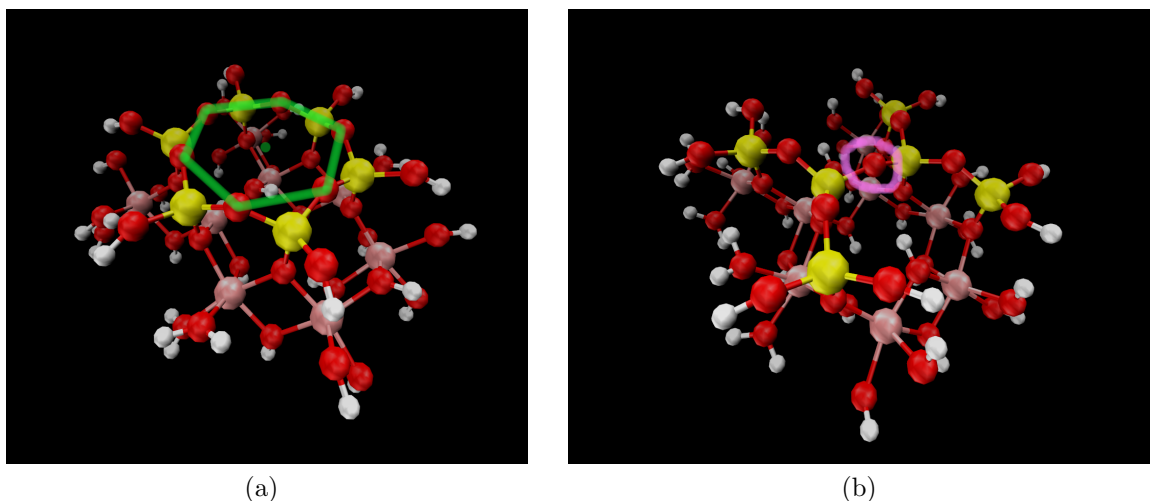


Figure 3.7: Montmorillonite clusters modeling the hexagonal, Figure 3.7a and oxygen site 3.7b. H (white), O (red), Al (pink) and Si (yellow).

We can consider to be three sites of interaction with the surface: a hexagonal site, a triangular site and direct interactions with oxygen atoms of the clay surface (oxygen site) (see Figure 3.6). The orientation of the aquaion must also be taken into account since it should have the freedom to rotate in solution. Due to the high cost of the calculations involved, we studied two sites, the hexagonal and the direct oxygen interaction. The QM calculations of the first were used as a training set to fit the HIC potential and then the QM calculations of the second were used as a control to check if in a very different type of site the potential was adequate.

In order to model the surface we built small clusters derived of the two surface sites. QM calculations of clay-clusters interacting with $[\text{UO}_2 \cdot (\text{H}_2\text{O})_5]^{2+}$ had already been reported in the literature.^{51,52} First of all, we considered clusters without Mg^{2+} cations. They are hard ions and in the CLAYFF their van der Waals interactions are

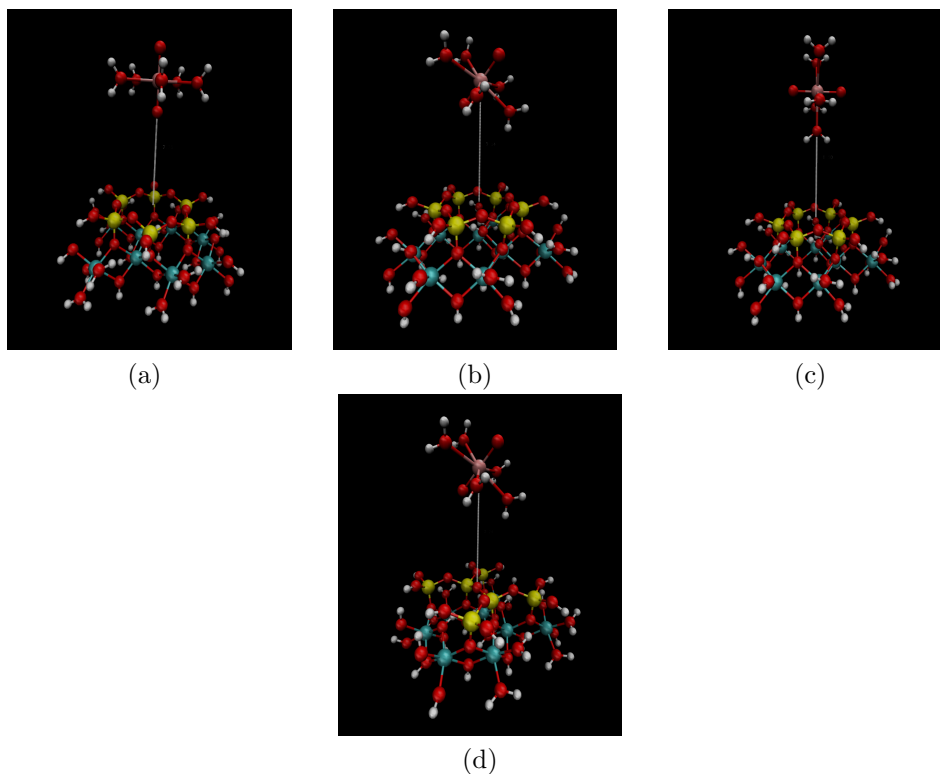


Figure 3.8: Clusters-aquaion scans used to parametrize the HIC interaction. Figures 3.8a-c represent the hexagonal site scan with tilt angles: 0° , 45° , 180° . Figures 3.8d represent the O-site scan with tilt angles: 45° . H (white), O (red), Al (turquoise), Si (yellow) and U (pink).

basically repulsive. Therefore, it is reasonable to think that their interaction with the $[\text{UO}_2 \cdot (\text{H}_2\text{O})_5]^{2+}$ is purely electrostatic. To deal with clusters of reasonable size, they contained a part of the tetrahedral Si layer and the octahedral Al layer but not the last Si layer. The cluster was cut out of the crystal structure and the relative atomic positions were not varied or optimized. The aluminosilicate cluster was then saturated with H atoms to make it closed shell and neutral. The two surface clusters can be seen in Figure 3.7. The hexagonal cluster has 98 atoms and the O site cluster has 101 atoms.

For the training set of QM single point calculations, scans where the aquaion approaches vertically on the geometrical center of the surface O hexagon were performed. They were computed with three orientations of the UO_2^{2+} , forming 0° , 45° and 180° (scans 1 to 3) angles with respect to the surface as sketched in Figures 3.8a to 3.8c. The distance, z from the closer O_{vl} to the clay surface ranged from 0 \AA to $13\text{-}15 \text{ \AA}$ depending on the point in which the classical electrostatic interaction and the QM interaction converge. The scan step was 0.25 \AA for $z < 6.0 \text{ \AA}$ and for $z > 6.0 \text{ \AA}$, 1 \AA . In all calculations,

the aquaion was kept in its optimized geometry. The control single points of the O-site cluster- $[\text{UO}_2 \cdot (\text{H}_2\text{O})_5]^{2+}$ interaction were carried out with a single scan with a 45° angle (scan 4, Figure 3.8d).

All QM calculations were carried out using *ORCA*,⁵³ at MP2 level using the frozen core approximation. For U, Si, Al the Stuttgart semirelativistic pseudopotentials were added to remove respectively 60, 10 and 10 electrons from the core and the rest were treated with basis sets [14s13p10d8f6g], [10s9p5d4f3g], [4s4p][2s2p] and [4s4p][2s2p] respectively.^{48,54} The rest of atoms are treated with Dunning’s aug-PVDZ basis set.⁴⁹ The basis set superposition uncertainty was neglected since it is very likely that the fitting procedure introduces more error in the classical interactions obtained than the basis set superposition error.

The interaction energy for a given aggregate structure, i , to be fitted was defined by the following relation:

$$E_{\text{int}}^i = E_{[\text{UO}_2 \cdot (\text{H}_2\text{O})_5]^{2+} - \text{clay}}^i - E_{[\text{UO}_2 \cdot (\text{H}_2\text{O})_5]^{2+}} - E_{\text{clay}} \quad (3.10)$$

In the aggregate, the optimized geometry of $[\text{UO}_2 \cdot (\text{H}_2\text{O})_5]^{2+}$ and the clay geometry cut out of the crystal structure were used. What changes for each aggregate is the distance and orientation of the aquaion. In our model force field equation the pure coulomb electrostatic interaction was considered to be separable from the non-coulomb term. This term is mostly van der Waals interactions but also includes implicitly into the parametrization for the aquaion-clay polarization and other many-body effects that come out of the QM interaction.

$$E_{\text{int}}^i = E_{\text{Coul.}}^i + E_{\text{non-Coul.}}^i \quad (3.11)$$

The ideal way to calculate the coulomb term of the interaction would be to calculate it using the CLAFF effective charges. Unfortunately, these charges are representative of the clay condensed phase and are different of those of the gas phase clay cluster. Therefore, the coulomb interaction was calculated for each structure with the CHELPG⁵⁰ charges of the clay cluster in the gas phase and the HI model charges of the aquaion. Although the CHELPG charges used to parametrize the HIC interaction are different of those in the CLAYFF, we must use in the simulation the original charges of the CLAYFF in order to represent correctly the intra-clay and clay-solution interactions. Since the coulomb term is considered to be separable from the non-coulomb term, we can take this last term obtained in a different context (gas phase cluster interactions) to the target system. The charges obtained from the gas phase clay cluster are similar on average to those of CLAYFF. This supports the integrability of the CLAYFF, the HI model and HIC interaction.

The non-coulomb interaction is fitted to the difference between the QM interaction energy and the classical electrostatic term calculated with the CHELPG charges. We modeled this HIC interaction as only containing interactions between the U, O_{y1} and O_{w1} (first shell water O) with the O and O_H (hydroxyl oxygen) of the clay, to which we shall refer collectively as O_{clay}. The cluster's O and O_H are given the same non-coulomb interaction since it is reasonable to think that their interactions with the aquaion are similar. In fact, the CLAYFF gives both the same Lennard-Jones parameters. The interactions between the Al, Mg, Si and H atoms of the clay with the aquaion are neglected since they are hard atoms and in the CLAYFF they are given negligible or 0 Lennard-Jones ϵ_{ii} . For the interactions between O_{y1} and O_{w1} and O_{clay} a 4 term r^{-n} polynomial was used like in the aquoion's HI model. For the case of the interaction of the clay with the U atom it is necessary to change the interaction's functional form making it very local and closer to a repulsive wall due to the high partial charge of the actinide atom that limits its capability for dispersion interactions. Therefore it was fitted to a 12-10 potential. The full HIC is presented below:

$$\begin{aligned}
 E_{\text{int}} = & \sum_i^{\text{aquaion}} \sum_j^{\text{clay}} \frac{q_i q_j}{r_{ij}} + \sum_i^{\text{O}_{\text{clay}}} \frac{C_{10}^{iU}}{r_{iU}^{10}} + \frac{C_{12}^{iU}}{r_{iU}^{12}} \\
 & + \sum_i^{\text{O}_{y1} \text{ and } \text{O}_{w1}} \sum_j^{\text{O}_{\text{clay}}} \frac{C_4^{ij}}{r_{ij}^4} + \frac{C_6^{ij}}{r_{ij}^6} + \frac{C_8^{ij}}{r_{ij}^8} + \frac{C_{12}^{ij}}{r_{ij}^{12}}
 \end{aligned} \tag{3.12}$$

3.3 Molecular Dynamics Simulations

All molecular dynamics simulations were done using *DL-POLY*.⁵⁵ The force fields and the system described previously were used. The simulation integrator was *Velocity Verlet*. For the rotational motion of the rigid bodies (the water molecules and the hydroxyl O_H-H units) the Euler equations of motion are integrated through quaternions with the NOQUISH algorithm. The integration time step chosen was 1 fs. PBC were applied and the Smoothed Particle Mesh Ewald technique (equivalent to the Ewald Sum) was used to calculate the electrostatic interactions. The van der Waals interactions were truncated at a cutoff radius of 14 Å. To set the average simulation temperature of the system to 300 K the Nose-Hoover thermostat was applied with a characteristic time of 0.5 ps. For NPT simulations, in addition to the thermostat, the Nose-Hoover barostat with an orthorhombic constraint was applied with a characteristic time of 0.5 ps to keep the average pressure at

1 atm. The orthorhombic constraint does not allow the barostat to change the simulation box angles. Thus, only the diagonal terms of the stress tensor of the system are affected by the barostat.

The stages of the molecular dynamics simulations were:

1. System minimization.
2. Thermalization: 200 ps of equilibration with temperature scaling every 0.2 ps and 500 ps of NVT production.
3. NPT simulations: 200 ps of equilibration with scaling every 0.2 ps and 2 ns of NPT production.

Unless otherwise stated all properties were studied for the production part of the NPT simulations.

3.3.1 Molecular Dynamics Properties

The radial distribution functions (RDF) , $g_{\alpha\beta}(r)$ of the system were studied. They are a measure of the probability of finding an β particle at a distance r of a α particle relative to the same probability in a homogeneous distribution. It can be used to define hydration shells as peaks of high probability of finding water molecules at certain distances of the metal. The coordination number would then be related to integral of $g_{U-O_w}(r)$ over the peak. It is defined according to the formula:

$$g_{\alpha\beta}(r) = \frac{n_{\alpha\beta}(r)}{\rho_{\beta}4\pi r^2\Delta r} \quad (3.13)$$

Where ρ_{β} is the numerical density of β particles, Δr is the histogram shell width and $n(r)_{\alpha\beta}$ is the radial number distribution of β around α . It is formally defined as:

$$n(r)_{\alpha\beta} = \left\langle \frac{1}{N_{\beta}} \sum_{i=1}^{N_{\alpha}} \sum_{j \neq i}^{N_{\beta}} \delta(|\vec{r} - \vec{r}_{ij}|) \right\rangle \quad (3.14)$$

Where $\delta(x)$ is the *Dirac delta function* and N_{β} the total number of β particles. The coordination number, n_{coor} is calculated with the following expression:

$$n_{\text{coor}} = \int_{\text{Shell Peak}} g_{\alpha\beta}(r)\rho_{\beta}4\pi r^2 dr \quad (3.15)$$

For the case of a heterogeneous system the ρ_β used to calculate $g_{\alpha\beta}(r)$ must be substituted by an effective density, ρ_β^{eff} that defines the true density that β is subject to. In the case of our montmorillonite the effective density of the hydration water is the water density of the interlayer and not the water density in the full simulation box since the water does not enter the layers. Thus, to calculate $g_{\alpha\beta}(r)$ we must use the water density in the clay interlayers.

Due to the laminal symmetry of the system under study it is interesting to study another structural distribution function which is the z -density function. It gives the average numerical density of an atom type, α at a given z value (in our simulation, the z -axis is perpendicular to the cell surface). We will use it to study the atoms average positions with respect to the clay surface. It is defined as:

$$\rho(r) = \frac{n(z)}{\frac{N}{z_{max}} \Delta z} \quad (3.16)$$

In our simulations we can also study dynamic properties of the particles. For example we can compute their autodiffusion coefficients, D_α . It can be measured using the Einstein formula for diffusion:

$$D_\alpha = \frac{1}{3d} \lim_{t \rightarrow \infty} \frac{d \langle r_\alpha^2(t) \rangle}{dt} \quad (3.17)$$

Where d is the number of dimensions of the diffusion motion and $\langle r^2(t) \rangle$ is the mean squared displacement (MSD) of atoms α . Apart from the diffusion in 3 dimensions the diffusion in the clay plane ($d = 2$) was also studied. The MSD can be calculated as follows:

$$\langle r_\alpha^2(t) \rangle = \left\langle \frac{1}{N_\alpha} \sum_i^{N_\alpha} |\vec{r}_i(t) - \vec{r}_i(0)|^2 \right\rangle \quad (3.18)$$

Another way to study the dynamics of the system is through its velocity autocorrelation function (VAC), $C(t)$, of the different atom types of the system. The VAC is a measure of the average change of the velocity vector of a particle in response to its surroundings. It gives an idea of how the velocity of a particle "loses memory" (decorrelates) of its original velocity. It is defined as:

$$C(t) = \frac{\langle \vec{v}(t) \cdot \vec{v}(0) \rangle}{\langle \vec{v}(0) \cdot \vec{v}(0) \rangle} \quad (3.19)$$

The VAC can be integrated to obtain the translational autodiffusion coefficient although it is more convenient to use the Einstein formula. An additional interesting

property derived from the VAC is its power spectrum which can be connected to the normal modes of molecular motion and is related to its classical vibrational spectra. The Fourier transform of the VAC provides the classical frequencies of the intramolecular and intermolecular normal modes. An interesting feature of these spectra is that these normal modes are not purely harmonic but include all the anharmonicity associated to them.

Chapter 4

Results and Discussion

4.1 HIC Interaction Parameters

The HIC interaction potential was developed in this project. The effective charges of this interaction potential are those of the $[\text{UO}_2 \cdot (\text{H}_2\text{O})_5]^{2+}$ and the clay's force field. The non-coulomb interaction potential parameters fitted to 103 QM single points are shown in Table 4.1.

Table 4.1: Coefficients from the fitting of the HIC interaction potential.

Coefficients	kcal mol ⁻¹ Å ⁻ⁿ	Coefficients	kcal mol ⁻¹ Å ⁻ⁿ
$C_4^{\text{O}_{\text{W1}}\text{O}_{\text{clay}}}$	-503.6	$C_4^{\text{O}_{\text{y1}}\text{O}_{\text{clay}}}$	606.2
$C_6^{\text{O}_{\text{W1}}\text{O}_{\text{clay}}}$	3181.8	$C_6^{\text{O}_{\text{y1}}\text{O}_{\text{clay}}}$	-15601.5
$C_8^{\text{O}_{\text{W1}}\text{O}_{\text{clay}}}$	11462.6	$C_8^{\text{O}_{\text{y1}}\text{O}_{\text{clay}}}$	112665.9
$C_{12}^{\text{O}_{\text{W1}}\text{O}_{\text{clay}}}$	-62929.4	$C_{12}^{\text{O}_{\text{y1}}\text{O}_{\text{clay}}}$	-287278.3
$C_{10}^{\text{UO}_{\text{clay}}}$	-8686428.6	σ	1.60 kcal mol ⁻¹
$C_{12}^{\text{UO}_{\text{clay}}}$	67323684.1	r	0.9995

In Figure 4.1 the interaction potential fitted coefficients of the HIC for the different atom types are collected. The U-O_{clay} potential energy well is very deep, very local (since it is 12-10 potential, see Equation 3.12) and has very abrupt rise to $+\infty$. Such an attractive potential well is a combination of the electrostatic contributions, dispersion interactions, polarization and other many body effects that an O_{clay} would suffer if it got close to the highly charged U atom. Since the partial charges of the coulomb interaction

are kept fixed during the fitting, the change in electron density due to the polarizing effect of U is introduced in the non-coulomb term.

O_{clay} interactions with the oxygen atoms of the aquaion are much weaker and can be thought to be closer to an induced dipole-induced dipole interaction. It is worth noting that the $O_{\text{yl}}-O_{\text{clay}}$ interaction energy is slightly positive even though tends to 0 as $r \rightarrow \infty$. This positive interaction, which if interpreted as a van der Waals interaction seems unphysical, is the result of compensation among interaction energies that if summed reproduce the total interaction energy. Furthermore, these compensations are a consequence of the fitting procedure which fits all pair interactions simultaneously to give the total interaction energy correctly. In this sense, one should bear in mind, that it is not possible to assign a physical interpretation to each pair interaction. Nevertheless, the total fitted interaction energy is completely physical as it is reproducing QM behavior of the system.

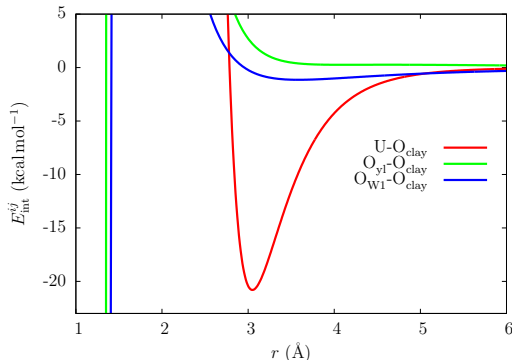


Figure 4.1: Pair potential interactions for the HIC model.

The correlation diagram in Figure 4.2 plots the QM interaction energy of every single point used to fit the potential (interaction with a hexagonal site calculations) against its interaction energy calculated by the classical potential fitted. We can see that the correlation is very good and there are no apparent biases in the fit. This shows that the HIC potential is well fitted (standard deviation, $\sigma = 1.60 \text{ kcal mol}^{-1}$, correlation coefficient, $r = 0.9995$).

Since the potential has been developed using a cluster model and using only one type of interaction site, it seems appropriate to see how the fitted potential describes the QM interaction energy for a different cluster modeling a different type of site than the one used to fit the HIC potential. For this reason, QM and HIC classical interaction energies of scan4 (described in Section 3.2.4) were computed. In this case, we are testing the

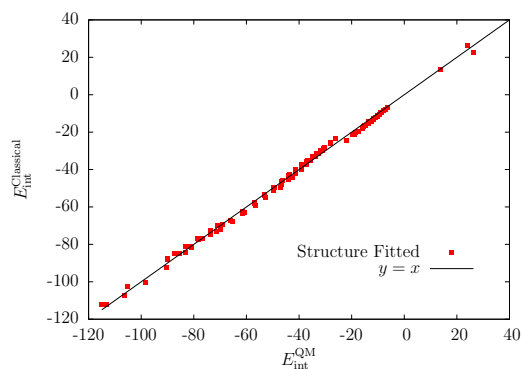


Figure 4.2: Correlation diagram for the fitted points of the HIC potential, single points modeling the interaction with hexagonal sites. $\sigma = 1.60 \text{ kcal mol}^{-1}$ and $r = 0.9995$

ability of the HIC potential to extrapolate the interaction energy in a range outside of that where it was fitted. The correlation diagram, Figure 4.3, shows that the potential extrapolates well to this new situation specially for the lowest interaction energy values which are the most visited in the simulation. This is corroborated by the correlation parameters $\sigma = 1.88 \text{ kcal mol}^{-1}$ and $r = 0.9970$. In conclusion, regardless of any possible interpretation of the pair potential energies, the HIC potential is capable of reproducing the modeled QM interaction satisfactorily.

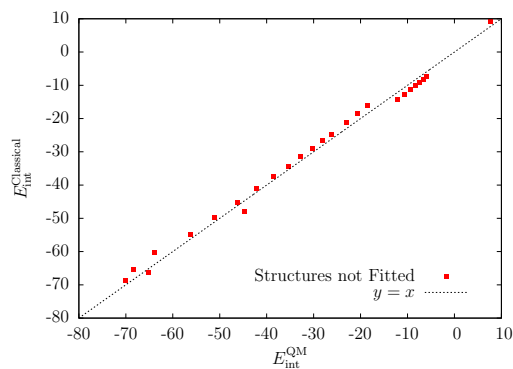
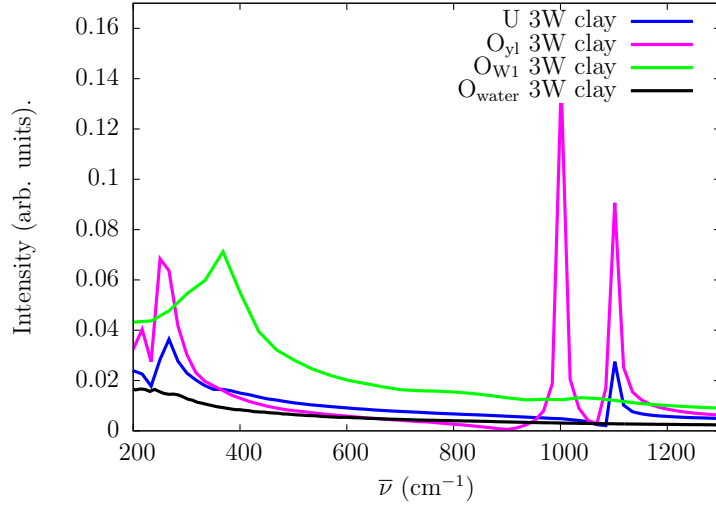
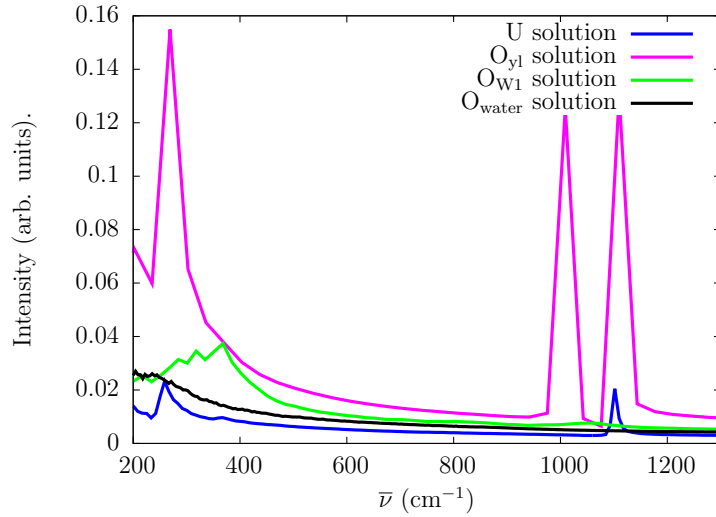


Figure 4.3: Correlation diagram for extrapolated points using the HIC potential, single points modeling the interaction with an O-site. $\sigma = 1.88 \text{ kcal mol}^{-1}$ and $r = 0.9970$



(a)



(b)

Figure 4.4: Fourier transforms of VAC for different atom types. Figure 4.4a corresponds to a 3W clay- UO_2^{2+} simulation and Figure 4.4b a aqueous solution of UO_2^{2+} using the HI model force field.

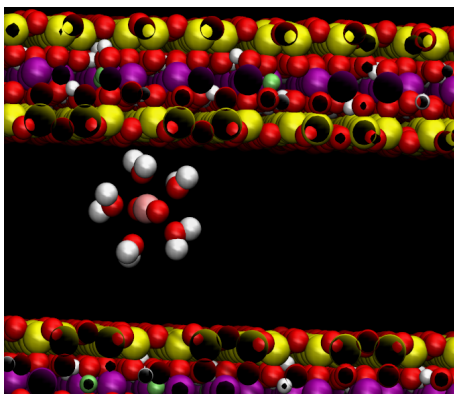
4.2 Velocity Autocorrelation Functions (VAC)

In Figure 4.4 the VAC power spectrum of the 3W clay and the aqueous solution of UO_2^{2+} simulations have been represented. The 4W VAC's fourier transform is not displayed since it is nearly identical to the 3W state one. Since the solution and clay VAC for the

represented atom types are equivalent, the introduction of $[\text{UO}_2 \cdot (\text{H}_2\text{O})_5]^{2+}$ inside the clay does not affect the intramolecular normal modes that were already observed in solution. Additionally no significantly different intermolecular normal modes can be seen in the broad regions found at low wavenumbers.

At 1100 cm^{-1} the A_2 symmetric tension of the UO_2^{2+} cation can be found in the power spectra of the two atoms participating in the normal mode. The $1A_1$ band at 1000 cm^{-1} corresponds to the symmetric tension of the cation and is only found in the O_{y1} atom power spectrum since U atom does not move in this mode. Around 360 cm^{-1} in the O_{W1} power spectrum we can find the $2A_1$ normal mode which corresponds to the symmetric tension of all five molecules in the equatorial plane. The UO_2^{2+} bending normal mode can be found at 260 cm^{-1} in the spectra of O_{y1} and U.

4.3 Simulation Visualizations



(a)

Figure 4.5: Simulation snapshot exemplifying the kind of outterphere complexes that are form. H (white), O (red), Mg (green), Al (purple), Si (yellow), U (pink). The H_2O and Na^+ are omitted for clarity.

From visualizations of the molecular dynamics simulations we can grasp some qualitative ideas about the behavior of the system. (The following ideas have been obtained from visualizing the 3W and 4W hydration states) It has been observed for the two simulations that the $\text{O}_{y1}\text{-U-O}_{y1}$ axis of the aquaion is at all times approximately parallel to the clay surface. The outersphere complexes that the aquaion forms with the clay surface is bound by the first hydration shell water molecules interacting through H-bonds with the surface O atoms. Figure 4.5 is an exemplifying snapshot of this behavior. It can be appreciated that the complex changes the first shell H_2O that directly binds to the surface frequently

by rotating about the O_{y1} -U- O_{y1} axis.

In the simulation time (2 ns) the $[UO_2 \cdot (H_2O)_5]^{2+}$ moves only slightly away from the surface to the center of the interlayer for small periods of time and returns to the same clay surface. The aquaions do not seem to change the surface they interact with.

The mechanism through which the aquaion diffuses in the clay plane (the xy plane) is a hopping mechanism.⁵⁶ In this type of diffusion mechanism the diffusing species interacts strongly with one site oscillating about a local equilibrium position for a while. When the species collects enough kinetic energy, it leaves the site and starts moving with a higher speed until reaching another site where it starts oscillating again. This behavior can be observed if we plot the coordinates of an U atom as a function of time in a 3W clay simulation, Figure 4.6. $z(t)$ only oscillates and is approximately constant because the aquaion is forming tightly bound outersphere complex with the surface and cannot move perpendicular to the clay layer. On the contrary, we can see that the x and y coordinates during some periods of time are oscillating but then move away from these positions into other sites where they begin to oscillate again.

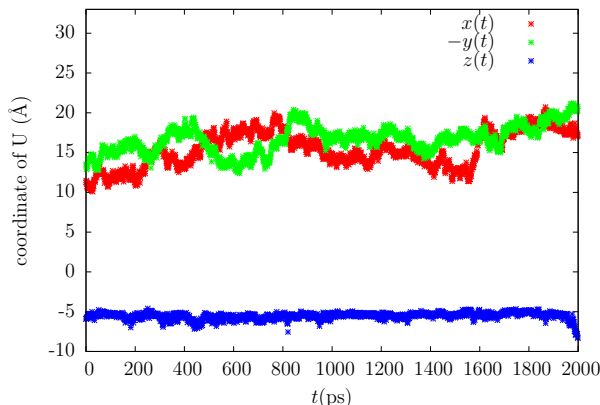


Figure 4.6: Cartesian coordinates as a function of time of a U atom in the 3W clay simulation to illustrate the hopping diffusion mechanism.

4.4 Radial Distribution Functions

In Figure 4.7 we present the RDFs obtained from the NPT simulations of this work and their comparison with the $[UO_2 \cdot (H_2O)_5]^{2+}$ aqueous solution RDFs using the HI model of UO_2^{2+} obtained from the literature.³⁵ A ρ_{eff} is used to calculate the RDFs of the montmorillonite systems using the water density within the interlayer and not the water density

of the whole simulation box. In the case of the O_{yl} RDFs the first hydration shell of the aquaion is omitted for clarity.

We can observe that the montmorillonite RDFs do not reach the limit value of 1 as in non-confined liquids. This is because at large distances when the ion influence on the solvent should become less important there are directions in space where water is excluded due to the presence of the clay. Thus, there is less water molecules at long distances of the cation than in a homogeneous system against which the RDFs are normalized. Therefore, the exclusion of water in some areas around the cation make RDF not tend asymptotically to 1.

The RDFs show that the first hydration shell which is fully flexible does not change its average structure significantly due to the confinement. We can also see that in between the second and third hydration shells the RDFs in all cases do not go to 0. This means that there is water exchange between these shells in the timescale of the simulation.

The position of the maxima of the second and third hydration shells for all montmorillonite simulations are very similar to the ones found in solution. This means that when entering the clay, the aquaion's hydration structure is barely affected by the presence of the clay and a confined solvent relative to solution.

Comparing the relative height of solvation shell peaks in different systems we can study the ordering capacity of the ion. The more defined and high the peaks are the stronger the ordering capacity is. The RDFs show that the ordering capacity of U for the second shell in solution and the two clay systems is the same. For the third hydration shell of U the RDFs of the solution system is already tending to one and the clay system RDFs cannot do so since water is excluded by the clay. Therefore, it can not be distinguished if the reason why the solution RDFs for the third hydration shell are higher than the clay RDFs due to a higher ordering capability of the cation or due to the exclusion of water in the clay layer. For the O_{yl} RDFs, on the other hand, the O_{yl} orders with the same strength in all three simulations for both the second and the third hydration shells.

Table 4.2: Coordination numbers for the montmorillonite and solution simulations.

Coordination Shell	Clay 3W	Clay 4W	Solution
2^{nd} U- O_{water}	27	25	30
2^{nd} U- H_{water}	62	58	66
2^{nd} O_{yl} - O_{water}	9	9	10
2^{nd} O_{yl} - H_{water}	17	17	18

The higher similarity of the RDFs of the clay and solution systems for O_{yl} RDFs with

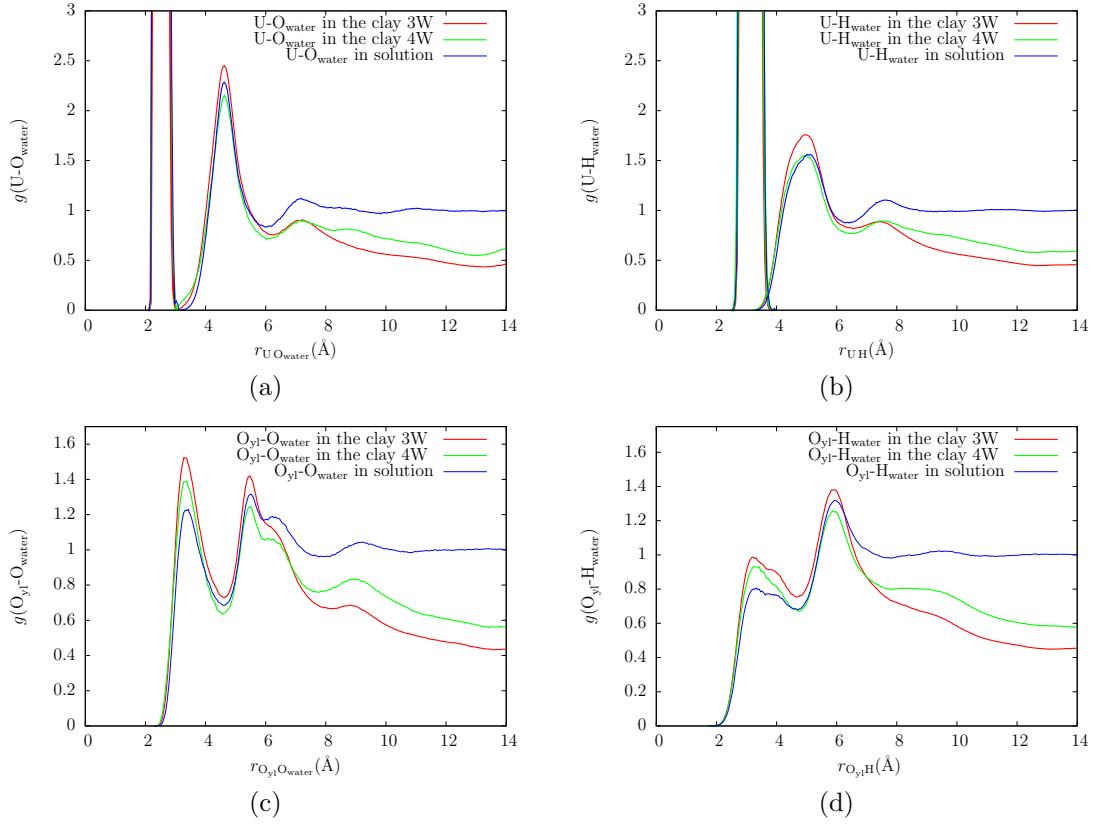


Figure 4.7: RDFs of $[\text{UO}_2 \cdot (\text{H}_2\text{O})_5]^{2+}$ in montmorillonite and solution. (a) $\text{U}-\text{O}_{\text{water}}$ RDFs, (b) $\text{U}-\text{H}_{\text{water}}$ RDFs, (c) $\text{O}_{\text{yl}}-\text{O}_{\text{water}}$ RDFs, (d) $\text{O}_{\text{yl}}-\text{H}_{\text{water}}$ RDFs. In the (c) and (d) the first shell of the aquaion is omitted for clarity.

respect to U RDFs, is because U RDFs reflect mostly the equatorial solvation of the aquaion and the O_{yl} RDFs the axial solvation of the ion.³⁵ Since in clay simulations the aquaion aligns the $\text{O}_{\text{yl}}-\text{U}-\text{O}_{\text{yl}}$ axis parallel to the clay surface, the equatorial hydration of the ion which is reflected more in the $\text{U}-\text{O}_{\text{yl}}$ RDFs is truncated by the clay surface because even first hydration shell is exposed to it. In contrast, the axial hydration is less affected by the clay because the O_{yl} is not directly in contact with the surface and the solution-clay similarity of the O_{yl} RDFs is extended up to the third hydration shell. This fact is supported by the coordination numbers as well.

In Table 4.2 the coordination numbers of the second hydration shells of the uranyl cation in montmorillonite and solution are presented. There is a dehydration process of the actinyl second hydration shell in its transit from solution to the mineral phase but only in its equatorial region since the O_{water} coordination numbers in solution and inside the clay are, for the clay hydration states considered, nearly the same. It is also worth

mentioning that the dehydration seems to be unaffected by the amount of water in the clay interlayer since the difference in coordination number of U for the clay in the 3W and 4W states is likely to be within the uncertainty of the coordination number calculation.

In conclusion, the UO_2^{2+} aquaion suffers a partial dehydration process when it enters the clay from solution. This dehydration occurs in its equatorial second hydration shell. The axial hydration of the aquaion is the same in the clay than in solution for the first three hydration shells. In contrast, the equatorial hydration shell's structure is disrupted by the clay in all shells except the first.

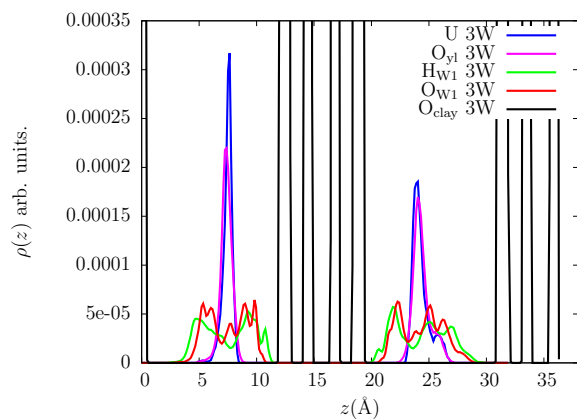
4.5 Z-Density Profiles

The Z-Density profiles obtained from the simulations give quantitative support to the qualitative behavior observed in the visualization. The sharp black peaks correspond to the O_{clay} atoms and thus the outermost peaks of each layer delimit the position of the solid surfaces. There is an overlap of the O_{yl} and U peaks which is indicative of the parallel disposition of the $\text{O}_{\text{yl}}\text{-U-O}_{\text{yl}}$ axis parallel to the clay surface. In addition, the peaks are close to one of the clay sheets with only small displacements towards the middle of the interlayer. The U-surface distance is approximately 4 Å with the first hydration shell in between. This is consistent with the experimentally observed outersphere complex formation.⁶

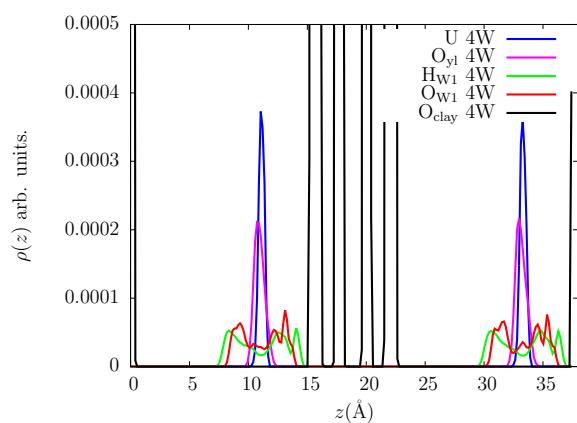
It is worth mentioning that the formation of an outersphere complex is not a consequence of any constraint that we have imposed on the system. The first shell water molecules are only bound in the first hydration shell by the interaction potential with the UO_2^{2+} cation. This potential imposes a high energy barriers for a water molecule to leave the first hydration shell that comes from the sampling and parametrization of the QM PES. But this energy barrier could be surpassed if the HIC potential was too strong and an innersphere complex or some other artefact be formed. Additionally, if the HIC potential was not attractive enough outterphere complexes would not be formed. Therefore, it a sign of robustness of the interaction potential fitted that we correctly reproduce the binding of the aquaion to the clay.

There is some difference between the 3W and 4W profiles. We can observe that the $[\text{UO}_2 \cdot (\text{H}_2\text{O})_5]^{2+}$ peaks for the 3W simulation are broader than the 4W one, showing that in the lower hydration state of the clay the aquaions are easier to displace from the surface. This is likely to be caused by the higher proximity of the other clay surface which attracts the aquaion with its electric field. This effect seems to overcome the reduced mobility

that the higher ionic strength of the 3W interlayer could produce since the higher the positive ion concentration the path a cation can move without being repelled by another is shorter.



(a)



(b)

Figure 4.8: Z-density profiles for UO_2^{2+} -clay simulations for the 3W and 4W hydration states for different atom types. The black lines that correspond to the O_{clay} atom delimit the position of the solid surfaces.

4.6 Translational Autodiffusion Coefficients of $[\text{UO}_2 \cdot (\text{H}_2\text{O})_5]^{2+}$ in montmorillonite

The autodiffusion coefficients of the uranyl aquaion were computed using the Einstein relation and are presented in Table 4.3. Two types of coefficients were calculated: three dimensional and two dimensional. In the last case, only motion in the clay plane was used to compute the MSD. The one dimensional translational autodiffusion coefficient in the z direction (perpendicular to the surface) is also given for comparison purposes but is only a crude approximation. They are only approximate because the simulations are not long enough for the ensemble average to reach the diffusion regime since there is not much motion in the z direction.

Direct measurement of translational autodiffusion coefficients in porous material is not possible experimentally. The experimental values of autodiffusion coefficients in porous materials are obtained using a model. What is experimentally measured is an apparent autodiffusion coefficient that with experimental modeling of the porosity and tortuosity (among other properties) of the material allow to obtain the autodiffusion coefficient (a microscopical property) from a macroscopic apparent autodiffusion coefficient.

The calculated D values for the clay simulations are within the range of experimental values of UO_2^{2+} diffusion in bentonite rock.

The comparison between our results and the experiment must be done with caution since our measurement is intrinsically microscopical and the experimental is derived from a macroscopical value using a model. Even though bentonite is mostly composed of montmorillonite, it is a complex material with several solid phases and a complicated structure difficulting to extrapolate the autodiffusion coefficient measured with the coefficient of a pure montmorillonite model system like the one studied in this work.

The theoretical values of D have been found to be nearly identical for the two clay hydration states studied for three dimensional and two dimensional diffusion. As expected, they are lower than aqueous solution coefficients by a factor of 5 due to the formation of a stable outersphere complex. Since this binding to the surface happens in one of the translational directions, excluding this coordinate and calculating the coefficient considering only motion in the plane, there should be an increase in its value. Unfortunately, the uncertainty in calculating autodiffusion coefficients in molecular dynamics simulation precludes to appreciate this effect. Nevertheless, the small values of the diffusion coefficient component perpendicular to the clay in comparison to the diffusion in the plane demonstrates that the aquaion motion happens mostly parallel to the surface. From the diffusion

data and other properties of the simulation, it can be concluded that the diffusion observed happens predominantly through motion parallel and close to the montmorillonite plane with a hopping mechanism and not in the middle of the interlayer.

Table 4.3: Autodiffusion Coefficients of $[\text{UO}_2 \cdot (\text{H}_2\text{O})_5]^{2+}$ in montmorillonite. The 2d D is calculated in the xy plane, the clay surface in our simulations and the 1d coefficient is calculated in the z direction, perpendicular to the surface.

$D(\times 10^{-5} \text{cm}^2 \text{s}^{-1})$	3 dimensions	2 dimensions	aprox. 1 dimension
Clay 3W	0.1 ± 0.1	0.2 ± 0.1	0.02
Clay 4W	0.1 ± 0.1	0.1 ± 0.1	0.004
Bentonite rock (exp.) ⁵⁷	0.095-0.28	-	-
Solution (HI model) ³⁵	0.5 ± 0.1	-	-
Solution (exp.) ⁵⁸	0.67 ± 0.01	-	-

Chapter 5

Conclusions

A first principles interaction potential for the $[\text{UO}_2 \cdot (\text{H}_2\text{O})_5]^{2+}$ -montmorillonite interaction has been developed. Further comparisons among quantum mechanical and interaction potential computations of the interaction energy for structural arrangements not considered in the fitting procedure support the robustness of the developed potential and its coupling with the clay and water models. The quantum mechanical force field was employed to run NPT molecular dynamics simulations on montmorillonite- $[\text{UO}_2 \cdot (\text{H}_2\text{O})_5]^{2+}$ systems with two different hydrations states. Several relevant structural and dynamical properties were extracted.

The VAC power spectra do not provide a way to distinguish any new intramolecular or intermolecular normal mode in the clay simulations with respect to the aqueous uranyl solution case. The power spectra computed for the clay simulations are essentially equivalent to those of solution.

The z-density profiles from the simulations allow concluding that in clay simulations outersphere complexes between the aquaion and the clay surface are formed without any external imposed constraint. This is consistent with the experimental evidence. Actinyl aquaions were not found to change the layer they were interacting with or to spend significant time in the interlayer during the time of our simulations. The 3W hydration state of the clay gives the cation a larger tendency of moving away from the layer because the opposite layer is closer than in the 4W case. The outersphere complex aligns its UO_2^{2+} axis parallel to the surface with the first shell water molecules interacting with the surface oxygen atoms.

U-O_{water} RDF profiles suggest a partial dehydration of the equatorial second hydration

shell of the actinyl cation with respect to its solution hydration structure. This is a consequence of the formation of a stable outersphere complexes. $O_{\text{yl}}-O_{\text{water}}$ RDF shows that UO_2^{2+} first hydration shell and its axial hydration shells are poorly affected by the presence of the solid surface. This is caused by the parallel orientation of UO_2^{2+} cation to the clay layer.

The computed theoretical autodiffusion coefficients are within the range of the experimental values for bentonite rock. The retention capacity of the clay is quantified in the simulations since the autodiffusion coefficients are lower by a factor of five than in aqueous solution. No significant differences in the coefficients were found for the two different clay hydration states studied. Due to the uncertainty in the calculation of D , no difference can be appreciated between two and three dimensional translational autodiffusion coefficients. Simulation results allow us to conclude that the $[\text{UO}_2 \cdot (\text{H}_2\text{O})_5]^{2+}$ diffusion happens mostly parallel and close to the clay plane through a hopping mechanism.

List of Figures

1.1	Geo. Disposal Facility	5
1.2	Na Montmorillonite clay	6
1.3	$\text{UO}_2^{2+}(\text{aq})$ complexes with montmorillonite	7
2.1	Frank and Evans concentric shell model.	8
2.2	Example calculation to construct a HIW potential.	12
2.3	$\text{UO}_2^{2+}(\text{aq})$ Hydrated Ion Model	13
3.1	Simulation boxes used in the study.	18
3.2	d_{001} simulated as a function $n\text{H}_2\text{O}$ per u.c.	18
3.3	TIP4P H_2O	20
3.4	Optimized structure of $[\text{UO}_2 \cdot (\text{H}_2\text{O})_5]^{2+}$	21
3.5	$[\text{UO}_2 \cdot (\text{H}_2\text{O})_5]^{2+}$ - H_2O PES sampling grid.	24
3.6	Montmorillonite surface sites for interaction.	25
3.7	Montmorillonite clusters.	25
3.8	Scans used to parametrize the HIC interaction.	26
4.1	Pair potential interactions for the HIC model.	33

4.2	Correlation diagram for the fitted points of the HIC potential.	34
4.3	Correlation diagram for the extrapolated single points of the HIC potential.	34
4.4	Velocity Autocorrelation Function Power Spectrum.	35
4.5	Simulation boxes used in the study.	36
4.6	$x(t)$, $y(t)$ and $z(t)$ of a U atom in the 3W clay simulation.	37
4.7	RDFs of $[\text{UO}_2 \cdot (\text{H}_2\text{O})_5]^{2+}$ in montmorillonite and solution.	39
4.8	Z-Density profiles of $[\text{UO}_2 \cdot (\text{H}_2\text{O})_5]^{2+}$ in montmorillonite and solution. . . .	41

Bibliography

- [1] Birkholzer, J.; Houseworth, J.; Tsang, C.-F. *Annual Review of Environment and Resources* **2012**, *37*, 79–106.
- [2] Denecke, M. A. *Coordination Chemistry Reviews* **2006**, *250*, 730 – 754, Actinide Chemistry.
- [3] Maher, K.; Bargar, J. R.; Brown, G. E. *Inorganic Chemistry* **2013**, *52*, 3510–3532, PMID: 23137032.
- [4] Knope, K. E.; Soderholm, L. *Chemical Reviews* **2013**, *113*, 944–994, PMID: 23101477.
- [5] Carretero, M.; Pozo, M. *Mineralogía aplicada*; 2007.
- [6] Catalano, J. G.; Jr., G. E. B. *Geochimica et Cosmochimica Acta* **2005**, *69*, 2995 – 3005.
- [7] Greathouse, J.; Cygan, R. In *Handbook of Clay Science*; Bergaya, F., Lagaly, G., Eds.; Developments in Clay Science; Elsevier, 2013; Vol. 5; pp 405 – 423.
- [8] Cygan, R. T.; Greathouse, J. A.; Heinz, H.; Kalinichev, A. G. *Journal of Materials Chemistry* **2009**, *19*, 2470–2481.
- [9] Skipper, N.; Refson, K.; McConnell, J. *The Journal of chemical physics* **1991**, *94*, 7434–7445.
- [10] Delville, A. *Langmuir* **1991**, *7*, 547–555.
- [11] Zhang, N.; Liu, X.; Li, C.; Liu, C. *Inorganic Chemistry Frontiers* **2015**, *2*, 67–74.
- [12] Greathouse, J. A.; Stellalevinsohn, H. R.; Denecke, M. A.; Bauer, A.; Pabalan, R. T. *Clays and clay minerals* **2005**, *53*, 278–286.

- [13] Greathouse, J. A.; Cygan, R. T. *Environmental science & technology* **2006**, *40*, 3865–3871.
- [14] Yang, W.; Zaoui, A. *Journal of Hazardous Materials* **2013**, *261*, 224 – 234.
- [15] Zaidan, O. F.; Greathouse, J. A.; Pabalan, R. T. *Clays and clay minerals* **2003**, *51*, 372–381.
- [16] Guilbaud, P.; Wipff, G. *The Journal of Physical Chemistry* **1993**, *97*, 5685–5692.
- [17] Böttcher, C.; van Belle, O.; Bordewijk, P.; Rip, A. *Theory of Electric Polarization*; Elsevier, 1973.
- [18] Barthel, J. M.; Krienke, H.; Kunz, W. *Physical chemistry of electrolyte solutions: modern aspects*; Springer Science & Business Media, 1998; Vol. 5.
- [19] Martell, A. E.; Hancock, R. D. *Metal complexes in aqueous solutions*; Springer Science & Business Media, 2013.
- [20] Burgess, J.; Burgess, J. *Metal ions in solution*; Ellis Horwood Chichester, 1978.
- [21] Marcus, Y. *Ion solvation*; Wiley, 1985.
- [22] Ohtaki, H.; Radnai, T. *Chemical Reviews* **1993**, *93*, 1157–1204.
- [23] Richens, D. T. *chemistry of aqua ions*; J. Wiley, 1997.
- [24] Frank, H. S.; Evans, M. W. *The Journal of Chemical Physics* **1945**, *13*, 507–532.
- [25] (a) Miertuš, S.; Scrocco, E.; Tomasi, J. *Chemical Physics* **1981**, *55*, 117–129; (b) Cances, E.; Mennucci, B.; Tomasi, J. *The Journal of Chemical Physics* **1997**, *107*, 3032–3041.
- [26] (a) Sanchez Marcos, E.; Pappalardo, R. R.; Rinaldi, D. *The Journal of Physical Chemistry* **1991**, *95*, 8928–8932; (b) Martínez, J. M.; Pappalardo, R. R.; Marcos, E. S. *The Journal of Physical Chemistry A* **1997**, *101*, 4444–4448.
- [27] Stockhausen, M. *Berichte der Bunsengesellschaft für physikalische Chemie* **1998**, *102*, 1521–1521.
- [28] Hansen, J.-P.; McDonald, I. R. *Theory of simple liquids*; Elsevier, 1990.
- [29] Sanchez Marcos, E.; Pappalardo, R. R.; Barthelat, J. C.; Xavier Gadea, F. *The Journal of Physical Chemistry* **1992**, *96*, 516–518.

- [30] Pappalardo, R. R.; Sanchez Marcos, E. *The Journal of Physical Chemistry* **1993**, *97*, 4500–4504.
- [31] Pappalardo, R. R.; Martínez, J. M.; Marcos, E. S. *The Journal of Physical Chemistry* **1996**, *100*, 11748–11754.
- [32] Galbis, E.; Hernández-Cobos, J.; den Auwer, C.; Le Naour, C.; Guillaumont, D.; Simoni, E.; Pappalardo, R. R.; Sánchez Marcos, E. *Angewandte Chemie* **2010**, *122*, 3899–3903.
- [33] Galbis, E.; Hernández-Cobos, J.; Pappalardo, R. R.; Marcos, E. S. *The Journal of Chemical Physics* **2014**, *140*, 214104.
- [34] Morales Negrito, N. Estudio teórico de propiedades fisicoquímicas de cationes metálicos en disolución: Evolución en el grupo de los alcalinos y en la serie de los lantánidos. Ph.D. thesis, Universidad de Sevilla, Spain, 2015.
- [35] Torrico Perdomo, F. M. Estudio Cuántico-Estadístico de la Hidratación de Cationes Hidratados. Ph.D. thesis, Universidad de Sevilla, Spain, 2005.
- [36] (a) Dunlap, B. I.; Connolly, J.; Sabin, J. *The Journal of Chemical Physics* **1979**, *71*, 3396–3402; (b) Van Alsenoy, C. *Journal of Computational Chemistry* **1988**, *9*, 620–626; (c) Kendall, R. A.; Früchtl, H. A. *Theoretical Chemistry Accounts* **1997**, *97*, 158–163; (d) Eichkorn, K.; Treutler, O.; Öhm, H.; Häser, M.; Ahlrichs, R. *Chemical Physics Letters* **1995**, *240*, 283 – 290; (e) Eichkorn, K.; Weigend, F.; Treutler, O.; Ahlrichs, R. *Theoretical Chemistry Accounts* **1997**, *97*, 119–124; (f) Ahlrichs, R. *Physical Chemistry Chemical Physics* **2004**, *6*, 5119–5121.
- [37] Neese, F.; Wennmohs, F.; Hansen, A.; Becker, U. *Chemical Physics* **2009**, *356*, 98 – 109, Moving Frontiers in Quantum Chemistry: Electron Correlation, Molecular Properties and Relativity.
- [38] Martinez, T. J.; Carter, E. A. Pseudospectral methods applied to the electron correlation problem. 1995.
- [39] Bickmore, B. R.; Rosso, K. M.; Nagy, K. L.; Cygan, R. T.; Tadanier, C. J. *Clays and Clay Minerals* **2003**, *51*, 359–371.
- [40] Loewenstein, W. *American Mineralogist* **1954**, *39*, 92–96.
- [41] Holmboe, M.; Bourg, I. C. *The Journal of Physical Chemistry C* **2014**, *118*, 1001–1013.

- [42] Holmboe, M.; Wold, S.; Jonsson, M. *Journal of contaminant hydrology* **2012**, *128*, 19–32.
- [43] Cygan, R. T.; Liang, J.-J.; Kalinichev, A. G. *The Journal of Physical Chemistry B* **2004**, *108*, 1255–1266.
- [44] Berendsen, H. J.; Postma, J. P.; van Gunsteren, W. F.; Hermans, J. **1981**, 331–342.
- [45] Jorgensen, W. L.; Chandrasekhar, J.; Madura, J. D.; Impey, R. W.; Klein, M. L. *The Journal of chemical physics* **1983**, *79*, 926–935.
- [46] Jensen, K. P.; Jorgensen, W. L. *Journal of Chemical Theory and Computation* **2006**, *2*, 1499–1509.
- [47] Frisch, M. J. et al. Gaussian 09 Revision D.01. Gaussian Inc. Wallingford CT 2009.
- [48] Cao, X.; Dolg, M. *Journal of Molecular Structure: THEOCHEM* **2004**, *673*, 203–209.
- [49] (a) Kendall, R. A.; Dunning Jr, T. H.; Harrison, R. J. *The Journal of chemical physics* **1992**, *96*, 6796–6806; (b) Woon, D. E.; Dunning Jr, T. H. *The Journal of chemical physics* **1994**, *100*, 2975–2988; (c) Woon, D. E.; Dunning Jr, T. H. *The Journal of chemical physics* **1993**, *98*, 1358–1371; (d) Kendall, R. A.; Dunning Jr, T. H.; Harrison, R. J. *The Journal of chemical physics* **1992**, *96*, 6796–6806.
- [50] Breneman, C. M.; Wiberg, K. B. *Journal of Computational Chemistry* **1990**, *11*, 361–373.
- [51] Tunega, D.; Haberhauer, G.; Gerzabek, M. H.; Lischka, H. *Langmuir* **2002**, *18*, 139–147.
- [52] Tunega, D.; Benco, L.; Haberhauer, G.; Gerzabek, M. H.; Lischka, H. *The Journal of Physical Chemistry B* **2002**, *106*, 11515–11525.
- [53] Neese, F. The ORCA program system. 2012.
- [54] Weigend, F.; Ahlrichs, R. *Physical Chemistry Chemical Physics* **2005**, *7*, 3297–3305.
- [55] Todorov, I. T.; Smith, W.; Trachenko, K.; Dove, M. T. *Journal of Materials Chemistry* **2006**, *16*, 1911–1918.
- [56] Smith, W. *Elements of Molecular Dynamics*; 2014; Chapter 3, pp 70–72.
- [57] Wang, X.; Chen, C.; Zhou, X.; Tan, X.; Hu, W. *Radiochimica Acta* **2005**, *93*, 273–278.

- [58] Simonin, J.-P.; Billard, I.; Hendrawan, H.; Bernard, O.; Lützenkirchen, K.; Sémon, L.
Physical Chemistry Chemical Physics **2003**, *5*, 520–527.